THESIS FOR THE DEGREE OF DOCTOR OF PHILOSOPHY

Detection and classification of sea ice from spaceborne multi-frequency synthetic aperture radar imagery and radar altimetry

WIEBKE ALDENHOFF

Department of Space, Earth and Environment
Division of Microwave and Optical Remote Sensing
CHALMERS UNIVERSITY OF TECHNOLOGY

Gothenburg, Sweden 2020

Detection and classification of sea ice from spaceborne multi-frequency synthetic aperture radar imagery and radar altimetry
WIEBKE ALDENHOFF
ISBN 978-91-7905-262-1

Doktorsavhandlingar vid Chalmers tekniska högskola
Ny serie nr. 4729
ISSN 0346-718X
Department of Space, Earth and Environment
Division of Microwave and Optical Remote Sensing
Chalmers University of Technology
SE-412 96 Gothenburg
Sweden
Telephone: +46 (0)31-772 1000

Cover:
Sentinel-1 C-band SAR image of sea ice in the Beaufort Sea overlayed with CryoSat-2 altimeter waveforms (not to scale). Multiyear sea ice floes (bright signature) are embedded in a matrix of first-year sea ice (dark signature). The blue line indicates the altimeter ground track. [Contains Copernicus Sentinel Data 2018].

Chalmers Reproservice
Gothenburg, Sweden 2020

Detection and classification of sea ice from spaceborne multi-frequency synthetic aperture radar imagery and radar altimetry

WIEBKE ALDENHOFF
Department of Space, Earth and Environment
Chalmers University of Technology

Abstract

The sea ice cover in the Arctic is undergoing drastic changes. Since the start of satellite observations by microwave remote sensing in the late 1970's, the maximum summer sea ice extent has been decreasing and thereby causing a generally thinner and younger sea ice cover. Spaceborne radar remote sensing facilitates the determination of sea ice properties in a changing climate with the high spatio-temporal resolution necessary for a better understanding of the ongoing processes as well as safe navigation and operation in ice infested waters.

The work presented in this thesis focuses on the one hand on synergies of multi-frequency spaceborne synthetic aperture radar (SAR) imagery for sea ice classification. On the other hand, the fusion of radar altimetry observations with near-coincidental SAR imagery is investigated for its potential to improve 3-dimensional sea ice information retrieval. Investigations of ice/water classification of C- and L-band SAR imagery with a feed-forward neural network demonstrated the capabilities of both frequencies to outline the sea ice edge with good accuracy. Classification results also indicate that a combination of both frequencies can improve the identification of thin ice areas within the ice pack compared to C-band alone. Incidence angle normalisation has proven to increase class separability of different ice types. Analysis of incidence angle dependence between 19–47° at co- and cross-polarisation from Sentinel-1 C-band images closed a gap in existing slope estimates at cross-polarisation for multiyear sea ice and confirms values obtained in other regions of the Arctic or with different sensors. Furthermore, it demonstrated that insufficient noise correction of the first subswath at cross-polarisation increased the slope estimates by 0.01 dB/1° for multiyear ice. The incidence angle dependence of the Sentinel-1 noise floor affected smoother first-year sea ice and made the first subswath unusable for reliable incidence angle estimates in those cases. Radar altimetry can complete the 2-dimensional sea ice picture with thickness information. By comparison of SAR imagery with altimeter waveforms from CryoSat-2, it is demonstrated that waveforms respond well to changes of the sea ice surface in the order of a few hundred metres to a few kilometres. Freeboard estimates do however not always correspond to these changes especially when mixtures of different ice types are found within the footprint. Homogeneous ice floes of about 10 km are necessary for robust averaged freeboard estimates.

The results demonstrate that multi-frequency and multi-sensor approaches open up for future improvements of sea ice retrievals from radar remote sensing techniques, but access to in-situ data training and validation will be critical.

Keywords: sea ice, SAR imaging, radar altimetry, sea ice concentration, sea ice classification, Fram Strait, Beaufort Sea

Acknowledgements

First and foremost, I would like to thank my examiner Lars Ulander and my main supervisor Leif Eriksson for giving me the opportunity to conduct not only this research but also gain experiences from international conferences, courses abroad as well as a research cruise to the Arctic. I also thank my assistant supervisor Céline Heuzé for her encouragement and motivation as well as quick responses. This research would also not have been possible without funding from the Swedish National Space Agency and the support of the administrative staff at the Department of Space, Earth and Environment.

Working would not have been the same without my current and former colleagues at the radar remote sensing group. They were always helpful not only in research questions but also to distract my mind and philosophise about life. Thanks to: Anders and Anders, Anis, Céline, Denis, Erik and Erik, Gisela, Jan, Lars, Maciej, Monika and Yufang. The rest of the department contributed to an environment and atmosphere that made it a pleasure to come to work and support was always available when needed. Sport with my teammates at LaBamba Frisbee Göteborg and Kungälvs Kanotklubb let me leave the office behind and gave me a lot of laughter, fun and memorable trips to tournaments.

Last but not least I would like to thank my family and friends for supporting me throughout my journey of life, bringing me back down to Earth when I got lost and all the memorable experiences outside of my working life.

Research contributions

This thesis is based on the work contained in the following papers:

Paper A W. Aldenhoff, A. Berg, and L. E. B. Eriksson. Sea ice concentration estimation from Sentinel-1 Synthetic Aperture Radar images over the Fram Strait. *IGARSS 2016 - 2016 IEEE International Geoscience and Remote Sensing Symposium*. IEEE, 2016, pp. 7675–7677. DOI: 10.1109/igarss.2016.7731001

Paper B W. Aldenhoff, C. Heuzé, and L. E. B. Eriksson. Comparison of ice/water classification in Fram Strait from C- and L-band SAR imagery. *Annals of Glaciology*, **59**(76pt2) (2018), pp. 112–123. DOI: 10.1017/aog.2018.7

Paper C W. Aldenhoff, L. E. B. Eriksson, Y. Ye, and C. Heuzé. First-year and Multiyear Sea Ice Incidence Angle Normalization of Dual-polarized Sentinel-1 SAR Images in the Beaufort Sea. *IEEE Journal of Selected Topics in Applied Earth Observations and Remote Sensing* (Accepted for publication)

Paper D W. Aldenhoff, L. E. B. Eriksson, and C. Heuzé. Comparison of Sentinel-1 SAR and Sentinel-3 Altimetry Data for Sea Ice Type Discrimination. *IGARSS 2019 - 2019 IEEE International Geoscience and Remote Sensing Symposium*. IEEE, 2019, pp. 4238–4240. DOI: 10.1109/igarss.2019.8899041

Paper E W. Aldenhoff, C. Heuzé, and L. E. B. Eriksson. Sensitivity of Radar Altimeter Waveform to Changes in Sea Ice Type at Resolution of Synthetic Aperture Radar. *Remote Sensing*, **11**(22), 2602 (2019). DOI: 10.3390/rs11222602

Other research contributions

Research contributions not included in the thesis:

- W. Aldenhoff. *Information Content of Multi-spectral SAR data – Sea Ice Classification - Test Case Fram Strait.* Tech. rep. Gothenburg, Sweden: Department of Space, Earth and Environment, Chalmers University of Technology, 2017

- Y. Ye, M. Shokr, S. Aaboe, W. Aldenhoff, L. E. B. Eriksson, G. Heygster, C. Melsheimer, and F. Girard-Ardhuin. Inter-comparison and evaluation of sea ice type concentration algorithms. *The Cryosphere Discussions* (2019). DOI: 10.5194/tc-2019-200

- C. Heuzé and W. Aldenhoff. Near-Real Time Detection of the Re-Opening of the Weddell Polynya, Antarctica, from Spaceborne Infrared Imagery. *IGARSS 2018 - 2018 IEEE International Geoscience and Remote Sensing Symposium.* 2018, pp. 5613–5616. DOI: 10.1109/IGARSS.2018.8518219

Contents

1 Introduction

The Arctic sea ice cover plays a key role in the global and regional climate systems. Sea ice acts as an insulator between the ocean and the atmosphere thereby regulating the exchange of heat and momentum [1]. The higher albedo, i.e. the ability to reflect solar radiation, of sea ice and especially its snow cover impedes the uptake of solar radiation by the ocean. A decrease of the fractional ice cover reduces the albedo and increased solar heating of the ocean further reduces the sea ice coverage and vice versa. This effect is known as the ice-albedo feedback loop [2]. Sea ice also forms a natural habitat for a unique flora and fauna [3] and is an essential part of the living environment of indigenous people. Figure 1.1 summarises the role of sea ice in the climate and ecological systems.

Changes of the sea ice cover therefore directly impact the local climate [4, 5] and imposes challenges on the vulnerable ecosystem of the Arctic Ocean [6]. Knowledge of the sea ice state is thus crucial for the understanding of ongoing processes and future predictions of the Arctic sea ice. The sea ice cover has been continuously and consistently monitored by spaceborne passive microwave radiometers on a daily basis since the late 1970's. Though interannual variability is large, a clear decrease of the yearly minimum sea ice extent and slight decrease of the maximum extent have been observed [7]. Figure 1.2 shows the median Arctic minimum sea ice extent from the satellite observations era (1981-2010) along the minimum sea ice extent 2019 provided by the National Snow and Ice Data Center (NSIDC) [8]. Moreover, the areal fraction of old multiyear sea ice, i.e. ice that has survived more than one summer's melt, has significantly been reduced since the start of the observations [9, 10]. The loss in multiyear sea ice and decrease in summer sea ice extent are concurrent with the reduction of mean sea ice thickness and hence the volume of the ice cover in the Arctic [11–13]. Thinning of the sea ice is also associated with an increase in sea ice drift speeds enhancing deformation and lead formation [14].

The retreating and thinning sea ice cover is not only one of the most visible signs of climate change but also increases accessibility of the Arctic for exploration and exploitation as well as commercial, scientific and touristic activities. The seasonal opening of northern shipping routes and exploitation of newly accessible fishing grounds have already increased the ship traffic in the Arctic [15, 16]. Navigation and offshore operations in ice infested waters require high resolution, in the order of a few hundred to a few tens of metres, and timely information of the sea ice

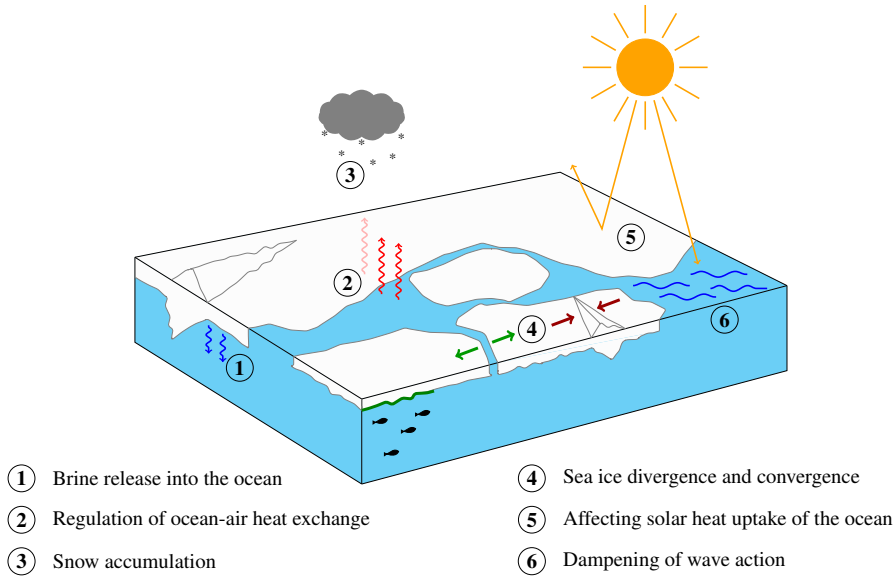

Figure 1.1: *Sea ice in the climate and ecological system.*

cover to minimise the risk of accidents and to protect the environment. Passive microwave radiometry used to derive the long-term climate time series of sea ice extent cannot meet these requirements regarding spatial resolution. Optical remote sensing techniques on the other hand provide the necessary resolution, but polar night and cloud coverage limit the use as data source for operational navigational information. Since the beginning of the 1990's spaceborne synthetic aperture radar (SAR) imagery has become the main source for higher spatial and temporal resolution information about the Arctic sea ice cover not only for operational and navigational purposes but also for studying local and regional variations of the sea ice cover [17]. Using electromagnetic radiation in the microwave region of the spectrum guarantees all year round and all weather observing capabilities, but interpretation of the imagery is not straight forward as the human visual system is trained for perception of optical information. Understanding the scattering of electromagnetic radiation from sea ice is therefore crucial for image interpretation. Radar is most sensitive to the surface and upper layer of the sea ice that undergoes constant changes induced by ambient conditions and ageing of the ice. Extensive research on radar scattering and in-situ observations has built the foundation of using SAR imagery to retrieve geophysical parameters of sea ice [18–20].

SAR imagery contains information about the sea ice type, e.g. new ice, young ice, first-year or multiyear ice, that is exploited for manual interpretation as well as automatic classification tasks to discriminate ice types or to identify leads [21–23]. Forced by wind and currents, sea ice is constantly moving creating for example ridges and leads by convergence and divergence of sea ice floes. Subsequent images of the same area enable motion estimation at high temporal and spatial resolution [24, 25].

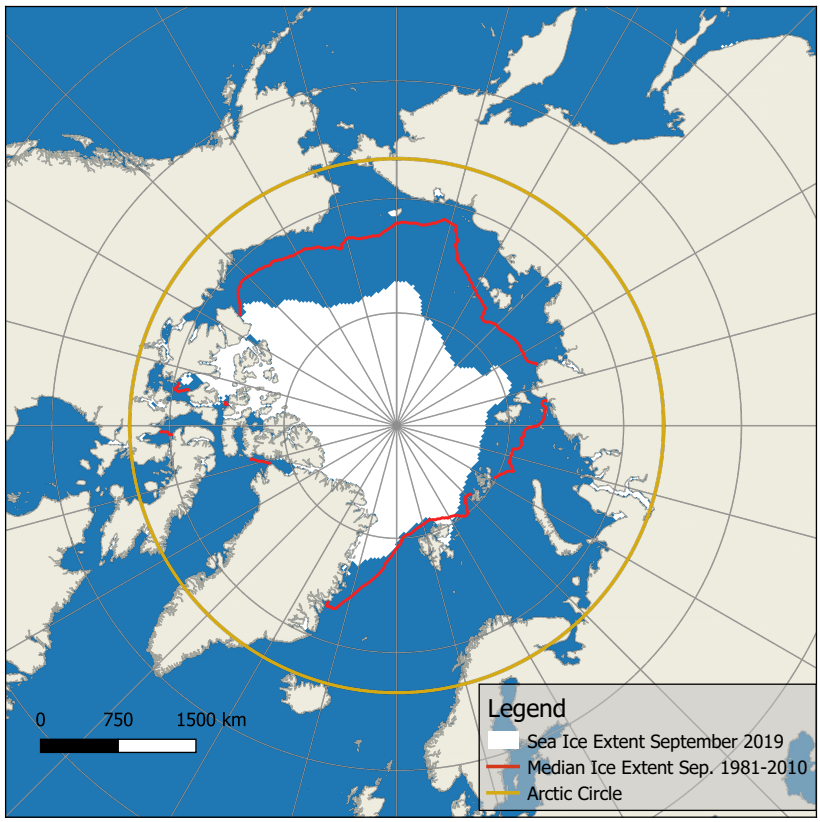

Figure 1.2: *Map of the Arctic with sea ice extent.*

Radar interferometry exploiting phase differences between two acquisitions is used to derive sea ice topography or stability of landfast ice [26, 27]. Sea ice thickness cannot be directly estimated from SAR imagery with sufficient accuracy [28, 29] but is of great interest both for climate research and navigation.

Sea ice thickness information has been scarce in space and time on the one hand because of the inaccessibility of the Arctic for in-situ measurements and on the other hand by limitations to retrieve sea ice thickness by means of remote sensing. Radar altimetry has long provided accurate information about sea surface height but large footprints and orbital constraints that excluded large parts of the central Arctic have limited the use for sea ice thickness measurements [30]. Promising results from altimeters on ERS-1/2 and Envisat [31, 32] and improvements in altimeter technology to reduce the along-track footprint size [33] led to the development of the CryoSat-2 mission dedicated to obtain sea ice thickness information up to high latitudes. Altimeter measurements from this mission allow sea ice thickness

retrievals on a continuous and Arctic wide basis [34].

Availability of radar remote sensing data and reference or ground truth data has in the past often been the limiting factor for research possibilities. This has drastically changed in recent years owing to more sensors in space and a more open data policy granting access to large amounts of data. The increased resources offer unique opportunities for not only spatially and temporally consistent observations but also for the intercomparison of different sensors that has often been impeded by large time lags. SAR imagery has long been an invaluable source as reference data for coarser resolution observations and verification of lead detection in altimeter measurements [35, 36]. Research of sea ice classification from spaceborne SAR imagery has so far focused on data from C-band. Though multi-frequency polarimetric data has been used in some studies for sea ice classification [37–39] little work has been done on wide swath imagery. Image resolution impacts the information content per unit area [40] and results therefore need to be validated for different resolutions. Altimeter measurements are to date mostly used for hemispherical weekly or monthly averaged maps of sea ice thickness [41, 42], albeit the introduction of the delay/Doppler altimeter improved the spatial resolution [33].

The main objective of this thesis is to investigate synergies of multi-frequency and multi-sensor radar remote sensing techniques for sea ice type and ice/water discrimination in the Arctic. Near-coincidental wide swath SAR imagery from Sentinel-1 at C-band and ALOS-2 PALSAR-2 at L-band are compared with respect to their individual classification capabilities either to complement the lack of data of one frequency or the potential gain of using a combination of the two different frequencies. Multi-sensor approaches focus on the combination of radar altimeter data and SAR imagery to evaluate the sensitivity of altimeter waveforms and associated freeboard estimates to small scale changes, i.e. hundreds of metres to a few kilometres, of the sea ice surface caused by variations in ice type or deformation features. Furthermore this comparison aims to create a basis for transferring the improved spatial resolution of delay/Doppler altimeters to ice thickness retrievals that are aided by ice type identification from SAR imagery.

The coming chapters provide the background knowledge necessary for the interpretation of the radar data as well as an introduction to the measurement principles of SAR images and radar altimetry. Furthermore, the work presented in the appended papers is set into context of past and current research and the addressed problems are outlined in more detail. The results of the papers are shortly summarised and are followed by a conclusion and an outlook to future research and challenges is given. The papers that form the thesis are presented in the appendix.

2 Microwave Scattering of Sea Ice

Observing the sea ice cover with active microwave instruments requires an understanding of the interaction of electromagnetic waves with the sea ice surface and volume. Scattering of electromagnetic waves depends on the one hand on the characteristics of the radar system and on the other hand on the properties of the sea ice. The radar system can be described by the frequency and polarisation, i.e. the orientation of the electric field vector relative to the surface, of the electromagnetic radiation as well as its observing geometry, i.e. incidence direction with respect to the surface. More information on the radar system is also given in Chapter 3. Sea ice properties of interest are surface roughness, volume composition and its dielectric characteristics. This chapter develops the background knowledge necessary for the interpretation of SAR images and altimeter waveforms.

2.1 Sea Ice

Sea ice is a complex heterogeneous and anisotropic medium that consists of freshwater ice, liquid brine inclusions, i.e. a highly saline solution trapped between ice crystals and air voids, and is additionally often covered by a layer of snow. It can be described by its physical, e.g. density, salinity and surface roughness, and dielectric, e.g. refractive index, properties. All these are highly variable in space and time and a complex function of amongst others sea ice age, its history and the ambient conditions. Radar scattering depends on the characteristics of the sea ice cover and changes induced by growth, ageing and deformation of sea ice are of importance for remote sensing. This section gives a brief overview of sea ice evolution relevant to sea ice remote sensing and is based on more rigorous descriptions that can be found for example in [43, 44].

In the context of this thesis three stages of sea ice evolution are of interest and their characteristic properties relevant for radar scattering are discussed in more detail:

1. Young ice
2. First-year ice
3. Multiyear ice

Young ice encompasses the first stages of sea ice formation from ice crystal growth to the consolidation of a more compact ice layer. Once the freezing point is reached in the upper layer of the ocean ice crystals start to form. This earliest step of ice formation is called frazil ice and accumulation of frazil ice crystals at the surface is called grease ice. Under calm ocean conditions these ice crystals consolidate to form a smooth, thin layer of sea ice known as nilas. These early stages of sea ice dampen and prevent the formation of capillary waves at the ocean surface. Furthermore, ice crystals consist of fresh water ice and the residual brine gets trapped within the ice layer or can accumulate beneath or at the surface of the ice sheet. On highly saline surfaces ice crystals can grow vertically at the ice-atmosphere interface and form so called frost flowers, crystalline ice structures a few centimetres in size. Formation of frost flowers increases the roughness of the otherwise smooth ice surface. Motion of the ice layer by wind, waves and current can lead to rafting, i.e. ice sheets are forced to slide over each other.

Under dynamic ocean conditions forced by wind and/or current interaction the formation of a homogeneous ice layer is not possible. Instead, ice crystals coalesce to form patches of accumulated ice. Under constant motion, these patches take a circular form with diameters up to 3 m. Their rims are usually raised by interaction with other floes and/or the deposition of frazil ice from the vicinity. This form of ice is named pancake ice after its appearance. Individual pancakes can freeze together under calmer conditions to form a more consolidated sheet of ice.

Under freezing conditions, the thickness of the ice constantly grows from the bottom of the ice sheet. This process is known as congelation and the ice transforms from young to first-year sea ice. Ice growth at this stage is controlled by the temperature gradient within the ice cover because of the insulating effect of the already formed ice layer and snow cover. Brine inclusions that were trapped within the ice during its formation get rejected under continuous ice growth by gravity drainage of the denser brine or brine expulsion, i.e. the increase in volume of ice compared to water exerts forces on the remaining brine that eventually gets expelled from the ice through small cracks [45]. Desalination in the bulk of the ice cover is the consequence of these processes. Furthermore the ice sheet is subject to constant forcing by wind, waves and currents that lead to divergence, i.e. lead formation, convergence, i.e. rafting and ridging, and shear processes. As ice thickens, mechanical properties of the ice sheet change from elastic at the early stages to a more brittle behaviour favouring ridging, i.e. the pile up of individual ice blocks, over rafting. Deformation processes greatly contribute to changes of sea ice roughness and ridges with a height of several metres can form. Additionally, a snow cover usually develops during the growth season.

Sea ice formation and growth is followed by the summer melt season. At first the wetness of the snow cover gradually increases. Refreezing of melt water or wet snow at the ice surface can form a layer of rough ice called superimposed ice. Eventually the snow cover disappears and the underlying ice is melted under the influence of the sun and warmer air temperatures. Water can accumulate in valleys forming so called melt ponds consisting of mostly fresh water. Refrozen melt ponds are relatively smooth compared to the surrounding ice. Ice that has survived at

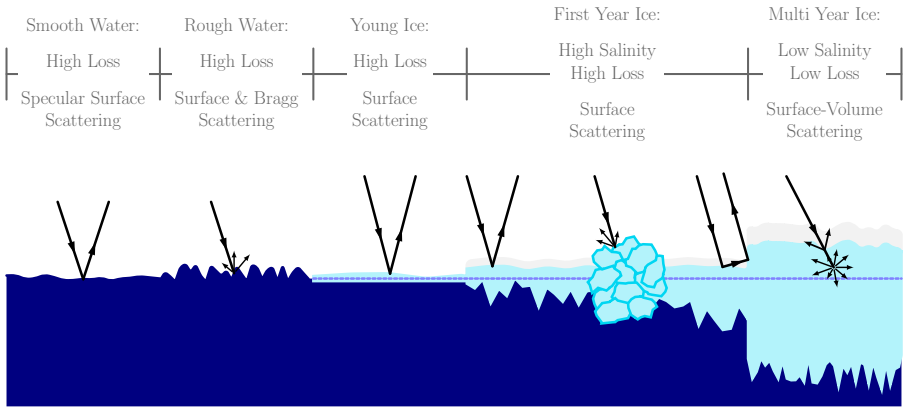

Figure 2.1: *Sea ice scattering mechanisms.*

least one summer's melt is termed multiyear sea ice throughout this thesis and therefore comprises second year and older sea ice. Melt and drainage processes have transformed the upper layer of this ice to have a low salinity and to contain numerous air bubbles. The density of multiyear sea ice is therefore lower compared to first-year sea ice [46].

2.2 Radar Scattering from Sea Ice

Scattering from sea ice is dependent on the properties of the ice itself and the characteristics of the observing radar system. As described in the previous section, the physical properties of the sea ice are changing during growth and ageing and are thereby affecting the involved scattering processes. Two main scattering mechanisms are distinguished: firstly, surface scattering, i.e scattering that occurs at the interface between two continuous media, and secondly volume scattering, i.e. scattering at dispersed inhomogeneities within a background medium. Figure 2.1 summarises the dominant scattering mechanisms for the main ice types and open ocean. The high dielectric contrast between the ocean and the air leads to a very small penetration depth of the radar wave into the water and scattering of calm and wind roughened water is therefore dominated by surface scattering. The high salinity of young and first-year ice favours surface scattering and prevents significant contributions from volume scattering. With increasing age, the salinity in the upper layer is reduced and microwave radiation can penetrate into the sea ice volume. Furthermore, the ice gets more porous by water percolation from the surface during the melt season, leaving a sufficient amount of air bubbles that act as scattering centres [47]. Volume scattering is therefore largely contributing to the total scattering signal of older sea ice at least for higher frequencies with wavelengths closer to the size of the scattering inhomogeneities.

Surface scattering is mostly dependent on the small scale roughness of the surface. Whether a surface is perceived as smooth or rough depends on the wavelength of

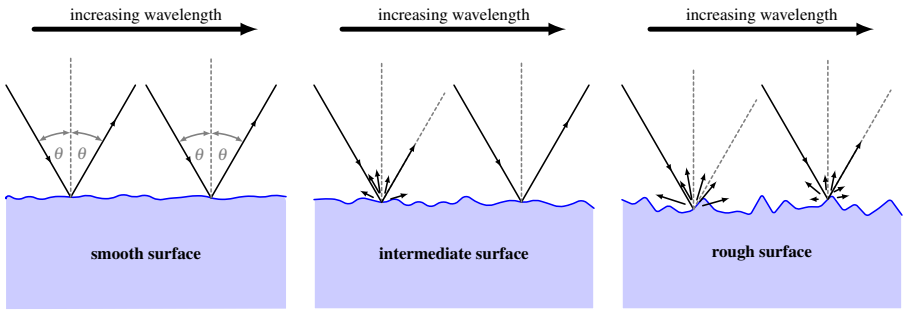

Figure 2.2: *Impact of increasing surface roughness on surface scattering at different frequencies.*

the microwave radiation. The Fraunhofer roughness criterion

$$s < \frac{\lambda}{32 \cos \theta} \tag{2.1}$$

with root mean square surface height s, wavelength λ and incidence angle θ is often used as a guideline for smooth surfaces [48]. Undulating surfaces are assumed to have a much larger wavelength than the microwave radiation. Smooth surfaces are dominated by coherent scattering, i.e. incidence and scattering angle are identical, and little to no depolarisation occurs. As surfaces get rougher, a noncoherent or diffuse scattering component, i.e. scattering in all possible directions, develops and depolarisation becomes more likely [49]. The effect of increasing surface roughness on scattering at different frequencies is shown in Figure 2.2. The roughness of the open ocean generally varies with the wind speed and can therefore span a wide range of values, starting from almost perfectly smooth for calm ocean areas and increasing in roughness with the wind speed. Capillary waves on the ocean surface with wavelength similar to the radar wavelength enable resonant Bragg scattering [50, 51]. Especially young ice is very variable in its surface roughness that is among other things depending on the wind conditions at its formation and the deformation history of the thin ice layer. After consolidation into a contiguous ice sheet, the surface remains relatively smooth but frost flower formation can greatly enhance small scale surface roughness. First-year ice stays relatively smooth but deformation features such as ridges have an increased surface roughness and significantly change the surface topography thereby enabling multiple scattering processes and creating facets directed in various directions. Multiyear sea ice often has an increased surface roughness caused by superimposed ice that formed during melt-freeze processes.

From the discussion of the different scattering processes it is apparent that the choice of the radar system parameters frequency, polarisation and incidence angle has an impact on the scattered signal. Frequency dependence is directly evident from Equation 2.1 for surface scattering. The wavelength of the radar frequency directly affects the backscattered signal which increases with the roughness of the surface. Volume scattering is determined by the size and distribution of the

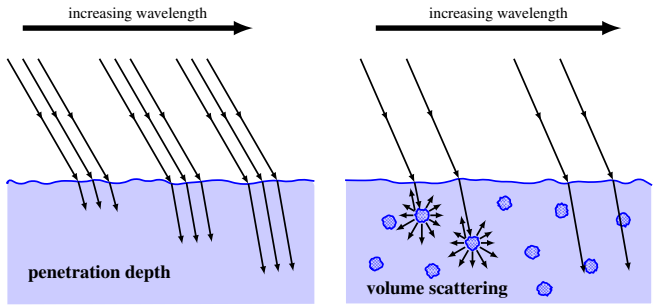

Figure 2.3: *Wavelength dependence of penetration depth (left) and volume scattering (right, scattering particle size exaggerated).*

air voids in the upper layer of the ice. The size of the air voids relative to the wavelength of the microwave radiation needs to be large enough to allow for effective volume scattering [20]. Furthermore, the frequency determines the penetration depth into a material and is usually larger for lower frequencies. These two cases are schematically emphasized in Figure 2.3.

Depolarisation, i.e. the change of the polarisation state, is mainly caused by multiple scattering characteristic for e.g. volume scattering, very rough surfaces or deformation structures [52]. Therefore especially the cross-polarised signal, i.e. polarisation of transmitted and received signal are different, can add additional information for sea ice classification tasks [21]. Of interest are the low depolarisation of scattering from the open ocean and the depolarisation differences between first-year and multiyear sea ice scattering. The incidence angle, i.e. the angle between the surface normal and the direction of the incoming radiation, affects the scattering process such that scattering usually decreases with an increasing incidence angle. This effect is less pronounced for the cross-polarised signal [19].

So far the discussion has neglected the influence of the snow layer that accumulates on the ice during winter. For dry snow conditions the impact of the snow layer is negligible for most radar frequencies [48]. For wet snow, however, the dielectric constant rapidly increases with moisture constant and surface scattering becomes more pronounced. Wet snow is also the reason why scattering signatures of different ice types vanish with the onset of melting, because the radiation can no longer penetrate into the ice layer.

3 Synthetic Aperture Radar Imaging of Sea Ice

Synthetic aperture radar (SAR) techniques enable monitoring of the Arctic sea ice cover with high temporal and spatial resolution independent of solar light and mostly undisturbed by clouds. SAR imagery has become the primary source of information about the sea ice cover for tasks that require timely and high resolution data but not necessarily daily global or hemispherical coverage. That is, for example, ice charting and navigation in ice infested waters. After a brief introduction to radar and SAR principles, SAR image interpretation with respect to sea ice information is discussed in more details in this chapter.

3.1 Radar Basics

Radar is an active remote sensing technique that transmits and receives radiation in the microwave region of the electromagnetic spectrum. For spaceborne sea ice observations this usually ranges from frequencies at about 1.2 GHz (L-band) to about 14 GHz (K_u-band) or equivalently for wavelengths from 25 cm to 2 cm. Besides its frequency, the electromagnetic radiation is described by the polarisation of the electric field vector. As shown in Figure 3.1, linear horizontal polarisation refers to an electric field vector oriented parallel to the xz-plane that contains the observed surface. For vertical polarisation the electric field vector is orthogonal to the propagation direction and the horizontal polarisation direction. Co-polarisation refers to using the same polarisation for transmitting and receiving, and is usually termed HH or VV for linear polarisation. Cross-polarisation employs different polarisation for transmission and reception and is denoted as HV or VH.

The radiation that is received back from a distributed target by the radar is given by

$$P_p^r(\theta,\phi) = \frac{P_q^t \lambda^2 G_0^2 A}{(4\pi)^3 R_0^4 L} \cdot \sigma_{pq}^0(\theta,\phi) \tag{3.1}$$

where P denotes power with transmit (t) and receive (r) polarisations q and p, λ the wavelength, G_0 the antenna gain factor, A the illuminated area, R_0 the range to the target, θ and ϕ determine the incidence direction in terms of incidence angle and azimuth direction respectively, L a loss factor and $\sigma_{pq}^0 = \frac{\langle \sigma_{pq} \rangle}{A}$ the backscattering coefficient with σ_{pq} the scattering cross section of a distributed target and $\langle \cdot \rangle$

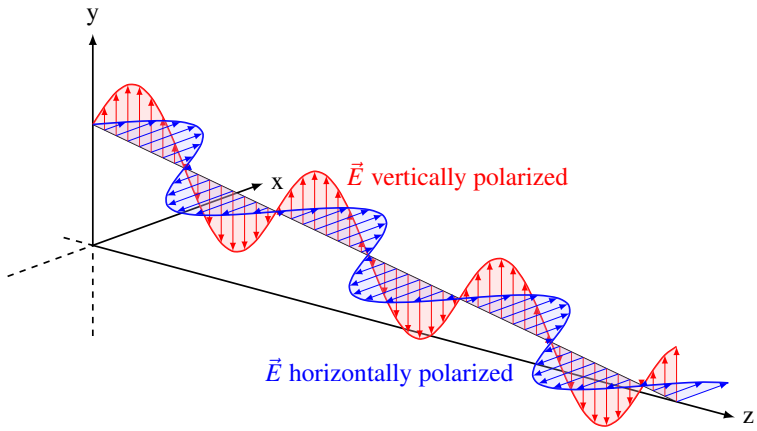

Figure 3.1: *Polarisation states of electromagnetic radiation.*

denoting the ensemble average. The ensemble average is taken into account because the power backscattered from a seemingly homogeneous distributed target exhibits large variations from one surface patch to another, which is known as radar speckle. Thus the power in Equation 3.1 should be interpreted as an ensemble average. The backscattering coefficient is the observable that links the target properties to the received power and thus contains the information available from radar imagery.

The incidence angle dependence of the backscattering coefficient σ^0_{pq} complicates the interpretation of the obtained measurements if large incidence angle ranges are covered by the data. It can partly be corrected by normalisation of the illuminated area to the incidence direction and therefore accounting for the changing illuminated area on the ground:

$$\gamma^0 = \frac{\sigma^0_{pq}}{cos(\theta)}. \tag{3.2}$$

Residual incidence angle dependence remains because of the explicit dependence of the backscattering coefficient $\sigma^0_{pq}(\theta, \phi)$ on the incidence direction. Model-based incidence angle correction is often used to obtain homogenised backscatter coefficients and thus to account for these variations [53].

Radar resolution in range for signals is determined by the bandwidth B of the signal

$$\delta_r = \frac{c}{2B}. \tag{3.3}$$

The spatial resolution of the radar system is dependent on the radar beamwidth in azimuth and elevation. The opening angle of the antenna can be approximated by the following equation [54]:

$$\theta_{ant} \approx \beta \cdot \frac{\lambda}{D}, \tag{3.4}$$

where β is a factor describing the antenna form, i.e. $\beta = 0.886$ for 3 dB width of a planar antenna with uniform weighting, and D is the antenna dimension with

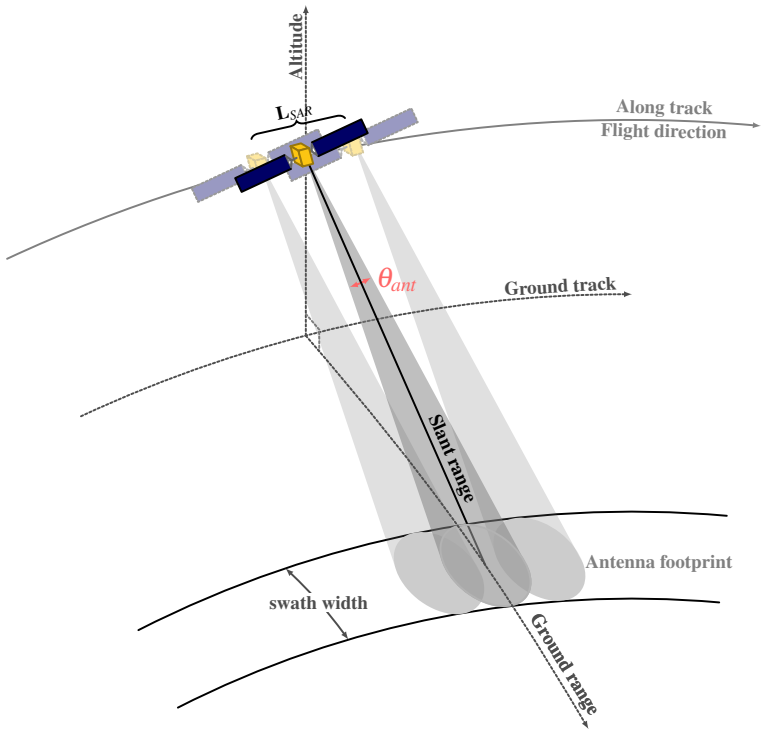

Figure 3.2: *SAR imaging geometry with L_{SAR} th elength of the synthetic aperture and θ_{ant} the opening angle of the antenna.*

$\lambda << D$. This results in an azimuth resolution that depends on the range from the antenna to the target:

$$\delta_{az} \approx \theta_{ant} \cdot R_{sl} \tag{3.5}$$

with the slant range R_{sl}.

3.2 Synthetic Aperture Radar Imaging

Conventional real aperture radar would require very large physical antenna sizes to obtain acceptable azimuth resolutions for spaceborne radar systems. SAR circumvents this problem by observing the ground from different antenna positions in space and thereby synthesising a large antenna and improving the azimuth resolution. A typical imaging geometry for the stripmap case is shown in Figure 3.2. A SAR system is a side-looking radar system with a look angle, i.e. the angle between nadir and the viewing direction, typically in the range of 15–55° for

spaceborne sensors. The direction along the antenna flight path is called along-track direction, the slant range is the distance between the antenna and the target and its direction is also termed across-track direction. The projection of the slant range onto the ground plane is called ground range. The 2-dimensional image space is spanned by the range or across-track dimension and the azimuth or along-track direction. The length of the synthetic antenna L_{SAR} is determined by the time a target is illuminated by the antenna.

The sequential observation of the target area from different antenna positions requires post-processing of the raw data to obtain a meaningful image. The following simplified view illustrates the general idea of SAR processing. At each antenna position a coherent linear frequency modulated pulse is transmitted. The received signal is stored in a 2-dimensional array where each antenna position is represented by a column which contains the range information. The range signal is compressed by applying a matched filter, i.e. the optimal linear filter that maximises the signal-to-noise ratio, to each column. In azimuth direction a target appears in a range bin according to its distance r_t from the antenna:

$$r_t(t) = \sqrt{r_0^2 + (v \cdot t)^2} \underset{\text{expansion}}{\overset{\text{Taylor}}{\approx}} r_0^2 + \frac{(v \cdot t)^2}{2r_0} \tag{3.6}$$

with r_0 minimal slant range to target, v the velocity of the antenna and t is time. The received signal in azimuth is proportional to:

$$s_{az}(t) \propto \exp\left(-j\frac{4\pi f_c r_t(t)}{c}\right) \tag{3.7}$$

where f_c is the centre frequency of the radar and c the speed of light. Inserting Equation 3.6 into Equation 3.7, the following expression is obtained:

$$s_{az}(t) \propto \exp\left(-j\frac{2\pi f_c (v \cdot t)^2}{c \cdot r_0}\right) \tag{3.8}$$

This is a linear frequency modulated signal in time and the azimuth resolution can be improved by range dependent matched filtering in azimuth direction assuming that a target remains in the same range bin [55]. If this is not the case, range cell migration occurs and need to be accounted for. Several different approaches have been invented to accommodate the problem and to minimize computational cost. A more rigorous treatment of SAR processing algorithms can be found in the following books [56–58].

The azimuth resolution of a SAR system can be expressed by [59]:

$$\delta_{az} = \frac{\lambda}{2\theta_{int}} \tag{3.9}$$

with wavelength λ and integration angle θ_{int}, i.e. the angle within which the target is illuminated by the antenna. Integration angles of different observation modes are shown in Figure 3.3. Stripmap mode is chosen if high resolution is required but on the expense of spatial coverage, while ScanSAR and variants like **T**errain

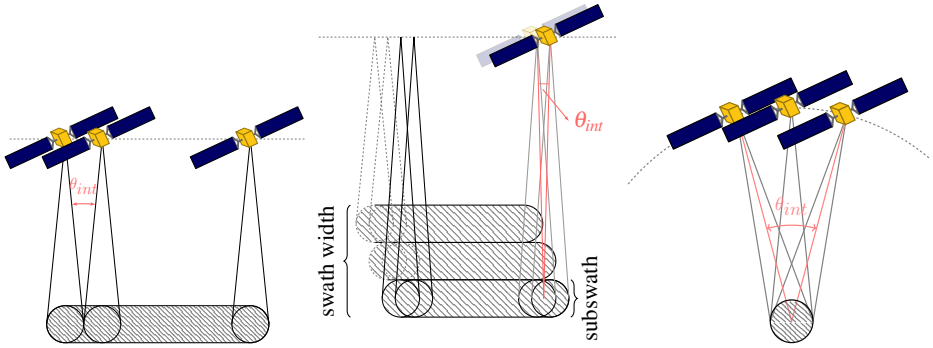

(a) *Stripmap* (b) *ScanSAR* (c) *Spotlight*

Figure 3.3: *Integration angles of different SAR modes*

Observation with **P**rogressive **S**can (TOPS) are typically used if spatial coverage is of interest. The latter ones are therefore widely used for sea ice observations. In the case of stripmap imaging the integration angle can be approximated by the antenna beamwidth (Equation 3.4) resulting in the widely used azimuth resolution formula:

$$\delta_{az} = \frac{D}{2}. \tag{3.10}$$

The resolution of a SAR system in azimuth direction is therefore independent of the range to the target. For ScanSAR acquisitions the azimuth resolution is smaller compared to stripmap mode because the full beamwidth is not used for image formation.

Resolution cells in SAR images represent a distributed target that consists of numerous elementary scatterers. The backscattered signal of such a resolution cell is therefore the coherent sum of all these scatterers. As no two resolution cells of a real but homogeneous surface have the exact same scatterer distribution this causes variations of the backscattered intensity from one resolution cell to another. This pixel to pixel variation is called speckle and causes a noisy or grainy image. In many imaging tasks it is desirable to reduce the effect of this noise like behaviour. Different filter techniques have been developed to preserve image structure and texture [60].

3.3 SAR image interpretation

Understanding the appearance of different sea ice types and open water is crucial for the interpretation of SAR imagery and the derivation of geophysical information. The side-looking geometry of the instrument lets smooth surfaces appear dark, i.e. very little backscattering to the system, and rougher surfaces or structures with oriented facets appear brighter in the imagery. Besides backscattering intensity different image areas can be distinguished by their texture, i.e. the spatial variation

of backscatter intensities, and contextual information, i.e. the surroundings of the area of interest [61].

Figure 3.4 shows an example of sea ice and open water at C-band (Sentinel-1) and L-band (ALOS-2 PALSAR-2) at co- and cross-polarisation. Backscatter levels at L-band are generally lower than at C-band where small scale surface roughness in the order of the radar wavelength creates higher backscatter levels. Evident from the images is that sea ice and open water are better distinguished at cross-polarisation. Scattering from the ocean surface is dominated by surface scattering and therefore backscattering is low at cross-polarisation. The contrast between sea ice and open water is, however, larger at C-band than at L-band [62]. Backscattering intensities over open ocean are more homogeneous compared to sea ice areas and hence show generally less texture. Geophysical phenomena, e.g. oceanic and atmospheric fronts or upwelling, can introduce some structure features to the backscatter of the ocean surface. Dark areas in open water are characterised by very smooth surfaces compared to the radar wavelength. Common causes are amongst others biogenic surface slicks or oil spills, new ice formation and wind shadowing that suppress capillary wave formation and therefore reduce radar backscatter [63]. Furthermore, backscatter intensities over open water are highly dependent on the incidence and azimuth angle as well as on the wind stress [64, 65]. Open ocean, therefore, spans a large range of possible backscatter values but its distinct texture that is usually homogeneous over large areas makes it discernible by visual inspection.

Sea ice also encompasses a wide variability of backscatter intensities and different textures driven by the stage of development and physical properties of the sea ice. Especially early stages of sea ice evolution exhibit large variations in radar backscatter depending on conditions under formation and exerted forces by winds and currents. Smooth ice surfaces of grease ice or nilas have a low backscatter intensity for the usual frequency range from X-band to L-band. Pancake and brash ice or ice that consists of individual floes below the resolution of the SAR system greatly increase backscatter intensities for shorter wavelength due to many facets that enable backscattering to the sensor. These ice types usually show very little texture with speckle-like backscatter. Frost flowers with sizes of a few centimetres greatly enhance small scale surface roughness and thus the backscatter intensity at higher frequencies [66]. Lower frequencies like L-band do not interact with these features and backscatter intensities are not increased [67]. Consolidated first-year sea ice has backscatter levels in between the low backscatter of smooth young ice and the high backscatter of roughened young ice.

Deformation features caused by convergence or shear of the sea ice increase the backscatter because of facets facing the radar and increased roughness of the surface. These effects are much more pronounced at L-band compared to C-band [68]. This is demonstrated by the area marked with a yellow ellipse in Figure 3.5. While at C-band no difference between the ice and deformation features is visible, these stick out at L-band as brighter features between darker ice floes. Thereby floe outlines are more clearly visible at L-band.

As sea ice ages, scattering from air voids within the sea ice volume becomes significant for smaller radar wavelengths or higher frequencies. Therefore, the

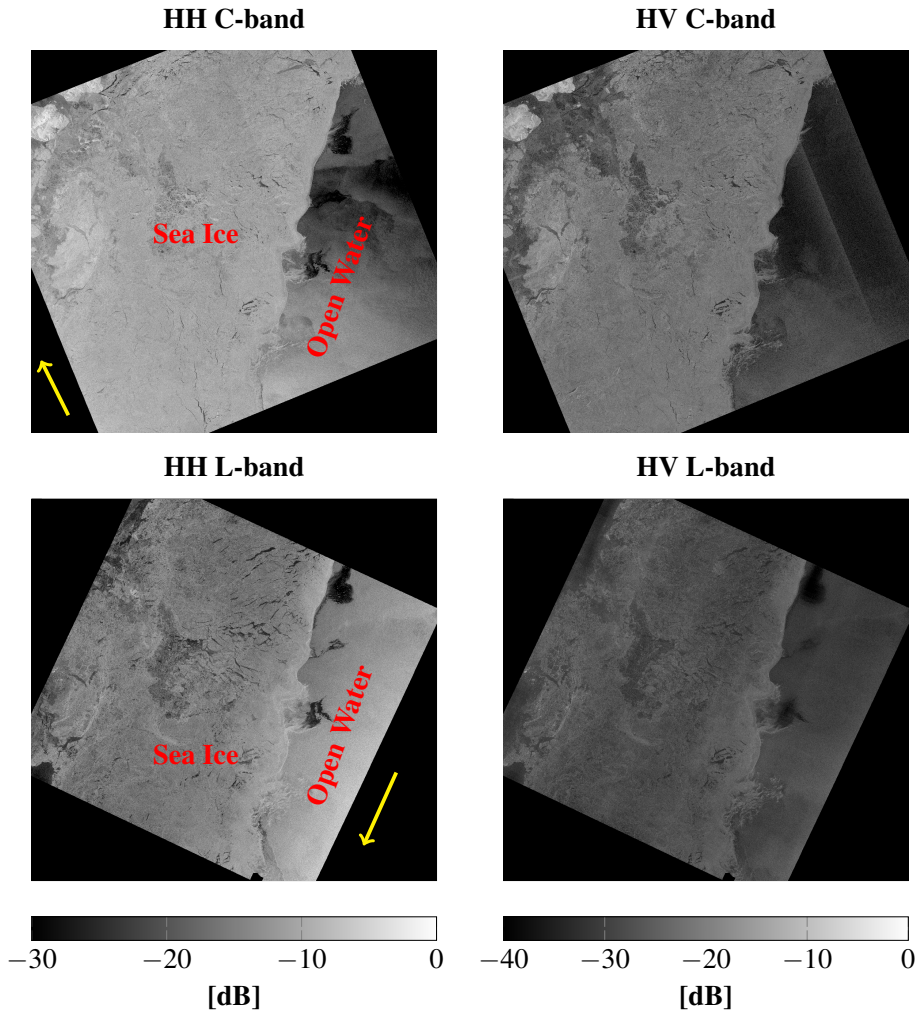

Figure 3.4: *SAR images of sea ice and open water taken on 2016-01-09 over Fram Strait. Top row: Sentinel-1 HH (left) and HV (right). Bottom row: ALOS-2 PALSAR-2 HH (left) and HV (right). Left and right colour bars refer to HH and HV images respectively. Yellow arrows mark the flight direction of the satellite. [Contains Copernicus Sentinel data 2016, ALOS-2 PALSAR-2 ©JAXA]*

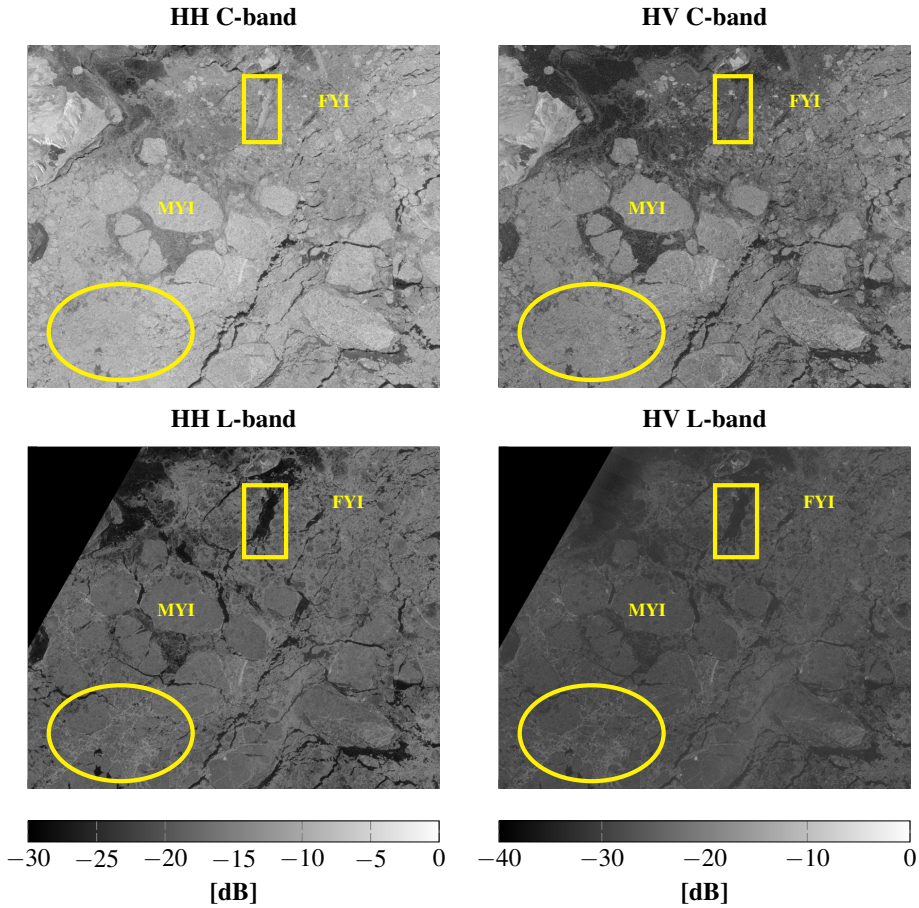

Figure 3.5: *SAR images of first-year and multiyear sea ice in Fram Strait 2015-10-22. Top row: Sentinel-1 HH (left) and HV (right). Bottom row: ALOS-2 PALSAR-2 HH (left) and HV (right). Left and right colour bars refer to HH and HV images respectively. Yellow ellipse and rectangle denote an area of enhanced ridging and of thin ice with increased small-scale roughness by possible frost flowers, respectively. A typical first-year ice area is marked with FYI and and old ice floe with MYI. [Contains Copernicus Sentinel data 2015, ALOS-2 PALSAR-2 ©JAXA]*

backscatter intensity of multiyear ice increases compared to the younger ice regimes. Longer wavelengths (lower frequencies) are, however, less sensitive to the small air inclusions and in addition to the larger penetration depths into the ice volume this leads to a reduced backscatter intensity of multiyear sea ice [69]. This effect is shown in Figure 3.5 at areas marked with MYI. From that figure, it is also notable that there is a larger contrast between multiyear sea ice and first-year ice at C-band than at L-band. Furthermore, the contrast between different ice types within the first-year ice area is enhanced in the C-band image. Areas of new ice formation (yellow rectangle in Figure 3.5) with possibly enhanced small-scale surface roughness by frost flowers appear bright at C-band while they remain dark at L-band. X-band backscatter intensities are similar to C-band but the shorter wavelength can increase the separation of first-year and multiyear sea ice [20, 70].

The preceding discussion focuses on differences during winter, when a cold and dry snow cover can be assumed that does not greatly affect the backscatter signal. This changes with the onset of melt when the larger penetration depth of L-band becomes beneficial for ice type separation during most of the melting season. Furthermore, during melt a reversion of the backscatter characteristics for first-year and multiyear sea ice, as described above, can be observed for C-band and L-band observations [71]. Generally summer conditions with a wet surface layer are challenging for radar remote sensing techniques as much of the surface contrast is lost.

3.4 SAR Missions and Data

Data of two spaceborne SAR missions has been used within this thesis: C-band Sentinel-1 and L-band ALOS-2 PALSAR-2.

Sentinel-1 is a constellation of two C-band SAR satellites that are part of the Copernicus Programme of the European commission providing long-term Earth observation data [72]. The first satellite, Sentinel-1A, was launched in 2014 followed by Sentinel-1B in 2016. Observations are today operational and follow a pre-planned acquisition schedule to fulfil the needs of the users. The radar frequency is 5.405 GHz corresponding to a wavelength of about 5.5 cm. A variety of observation modes provide different resolutions and spatial coverage. The predominant mode over the Arctic sea ice is the extra-wide swath mode in medium resolution with a swath-width of 400 km and a spatial resolution of about 100 m in range and azimuth. This data type has been used throughout this thesis. Usually the data is available as dual-polarisation imagery with horizontal receive and transmit (co-polarisation, HH) and horizontal transmit and vertical receive (cross-polarisation, HV). The noise equivalent sigma zero (NESZ), i.e. the noise floor of the images, is better than -22 dB but varies with incidence angle being lower for higher incidence angles. The cross-polarisation channel of images taken before 2018-03-13 show azimuthal scalloping noise. i.e. noise variations due to antenna pattern corrections, and noise artefacts at interswath boundaries for areas of low radar backscatter even after using the supplied noise correction information [73]. Scalloping noise and interswath boundary variations are greatly improved with the introduction of new

Table 3.1: Parameters of Sentinel-1 and ALOS-2 PALSAR-2 SAR images used in the scope of this thesis.

Mission	Mode	Swath width	Polarisation	Resolution (az/ground rg)	NESZ
Sentinel-1	EW GRDM	400 km	HH+HV	87 m/93 m	−22 dB
ALOS-2	ScanSAR	350 km	HH+HV	78 m/95 m	−26 dB

noise information after that date but over sea ice an increased backscatter of the first subswath remains [74].

ALOS-2 PALSAR-2 is an L-band SAR system operated by the Japan Aerospace Exploration Agency (JAXA) that was launched in 2014. The radar frequency is 1.26 GHz corresponding to a wavelength of about 24 cm. ScanSAR mode provides data with a swath width of 350 km and a spatial resolution of about 100 m in range and azimuth. Dual-polarisation data with HH and HV channels is used for the research in this thesis. The NESZ of the data is better than −26 dB. For imagery taken before 2018-04-11, the cross-polarisation channel can be blurred over areas with low backscatter intensities [75]. Sea ice observations from ALOS-2 PALSAR-2 are much more scarce in space and time than those available from C-band radar. Key parameters for imagery from Sentinel-1 and ALOS-2 PALSAR-2 used in the scope of this thesis are summarised in Table 3.1.

4 Radar Altimeter Observations

Radar altimeters are instruments to determine the height of the sensor above the scattering surface. In sea ice remote sensing this can be used to determine sea ice freeboard, i.e. the height of the ice above the water surface, and eventually sea ice thickness by assuming hydrostatic equilibrium. The following sections will present the principles of delay/Doppler (synthetic aperture radar) altimetry and an introduction to altimeter waveform interpretation of sea ice returns.

4.1 Delay/Doppler Altimetry

Radar altimeters are nadir-looking instruments that determine the distance or range from the sensor to the scattering surface by transmitting and receiving radar pulses. The range and spatial resolution of a radar altimeter are governed by the same principles as described in Section 3.1. Radar altimeters are, however, mostly operated in pulse-limited mode, that is the footprint on the ground is determined by the pulse length rather than the opening angle of the antenna. For distributed targets such as ocean and ice surfaces, the measured distance corresponds to a mean surface of all the scatterers within the footprint area. The resulting measurement is therefore susceptible to speckle noise and several pulses are averaged to obtain an accurate height measurement. This averaged signal is called a waveform and reflects received power depending on range from the antenna. A schematic of the observation geometry, the pulse limited footprint and the received waveform is shown on the left of Figure 4.1. The waveform shows an initial rise when the leading edge of the pulse is reflected by the surface and reaches its maximum when the trailing edge of the pulse is first reflected from the surface. The illuminated area at that time instance is a circle (depicted in blue on the left of Figure 4.1) and equivalent to the pulse limited footprint. Thereafter the illuminated area forms annuli of equal area. Theoretically the waveform would remain constant but decreases primarily because of antenna pattern weighting [76–78]. The pulse limited footprint of such conventional spaceborne radar altimeters is in the order of 1.5–2.5 km in diameter but can be significantly larger for rough seas [79, 80]. The beam-limited footprint is determined by the opening angle of the antenna and is on the order of 15 km.

Accurate height estimates require a homogeneous surface within the pulse limited footprint, which is not always expectable over sea ice. Therefore a new type

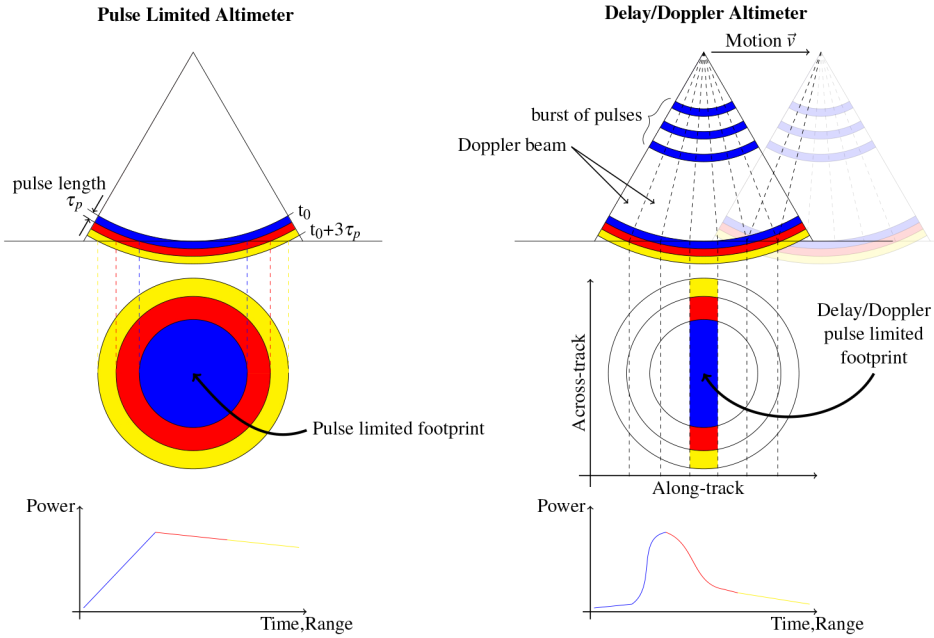

Figure 4.1: *Observation geometry, pulse limited footprint and waveform for conventional radar altimetry (left) and delay/Doppler or synthetic aperture radar altimeters (right) [adapted from [33]].*

of radar altimeters employs similar techniques to SAR imaging to reduce the along-track footprint size and are known as delay/Doppler or SAR altimeters [33]. The principle is schematically outlined on the right in Figure 4.1. A burst of coherent radar pulses is sent out and the received signal can be seen as a 2-dimensional data matrix. The range direction corresponds to a conventional waveform from each pulse and the azimuth direction to the antenna position where each pulse was sent. This signal can be split into Doppler beams or equivalently incidence angle that correspond to a distinct patch, i.e. ground cell, on the surface. The same ground cell is viewed for a number of bursts and due to the motion of the platform located at different Doppler beams or angles for each burst. After range correction the individual measurements of the same ground cell but from different bursts or viewing angles form a stack of measurements. The final signal is obtained by incoherently averaging over the stack and is called a multi-looked waveform. The delay/Doppler waveform is much more peaky compared to the conventional altimeter because the area contributing to the signal decreases with distance from the radar [33]. The along-track pulse limited footprint size of today's delay/Doppler altimeters is reduced to about 300 m [34].

The challenge of radar altimetry is to retrieve an accurate height measurement from the returned waveform. This process is called retracking. Common to all approaches is to determine the point on the leading edge of the waveform that

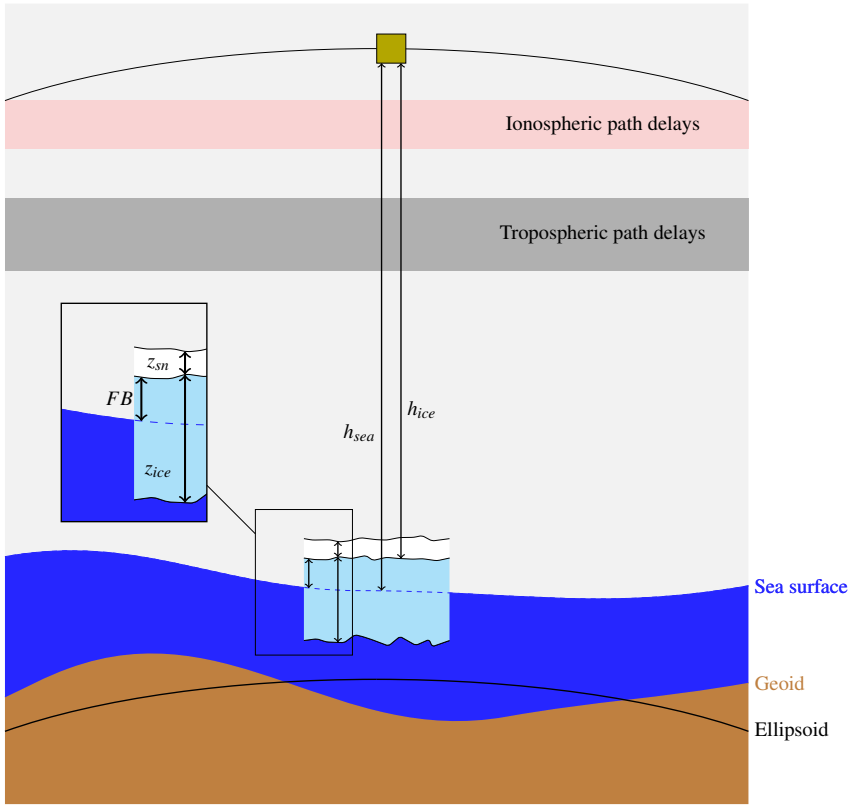

Figure 4.2: *Relations between range measurements and freeboard for radar altimetry. h_{ice} and h_{sea} are the range between the altimeter and sea ice surface and sea surface, respectively. FB is the ice freeboard and z_{sn} and z_{ice} the height of the snow layer and sea ice thickness respectively.*

corresponds to the closest distance from the sensor to the surface. This point is referred to as the retracking point. Different algorithms have been proposed for this task: empirical retrackers like threshold retrackers that determine the point on the leading edge by a threshold value [81–83] or retrackers that fit a model to the waveform [84, 85]. The obtained range is subject to instrumental, e.g oscillator drift or Doppler shift error, and geophysical, e.g wet and dry tropospheric as well as ionospheric, delay errors that need to be accounted for [78, 86, 87]. Corrections for these effects are usually provided with the data and are obtained from models of the atmosphere or measurements of complementary sensors [88]. Sea ice freeboard can be estimated by the difference between corrected range to the sea ice surface h_{ice} and the range to the local sea surface h_{sea} (see Figure 4.2):

$$FB = h_{sea} - h_{ice}. \tag{4.1}$$

The local sea surface can be determined from leads, i.e. openings within the ice

pack either revealing a calm sea surface or covered by thin ice. The radar scattering horizon over snow covered sea ice is, however, not necessarily equal to the snow-ice interface and imposes challenges for sea ice freeboard retrievals [89, 90]. The measured freeboard is therefore termed radar freeboard to discriminate it from the real freeboard [83]. Sea ice thickness z_{ice} can be calculated from freeboard assuming hydrostatic equilibrium [91]:

$$z_{ice} = FB\frac{\rho_w}{\rho_w - \rho_{ice}} + z_{sn}\frac{\rho_{sn}}{\rho_w - \rho_{ice}} \tag{4.2}$$

where FB is freeboard, z_{sn} the thickness of the snow layer and ρ_w, ρ_i and ρ_{sn} the density of water, ice and snow respectively. Ice density depends on the sea ice type and is lower for multiyear sea ice compared to first-year sea ice [92]. Knowledge of the ice type is thus crucial for accurate sea ice thickness estimates.

4.2 Waveform Interpretation

Accurate freeboard estimates require the separation of sea ice waveforms from those representing leads and open ocean or those that contain contaminations from mixed surfaces. Waveforms can be distinguished by different parameters that describe either the shape of the waveform or the stack of waveforms used to create the multi-looked waveform. The latter ones give information about the angular variation of power within the stack of waveforms that originates from the motion of the sensor between bursts [34]. Commonly used parameters are peak power, pulse peakiness, leading or trailing edge width and stack standard deviation, a measure of angular variation of power in the stack of waveforms. Pulse peakiness is commonly defined as the ratio of peak power to mean power [83, 93]:

$$PP = \frac{max(WF_i)}{\sum_i WF_i}N \tag{4.3}$$

where WF_i is waveform power in range bin i and N the number of range bins. The scaled inverse mean power (IMP) has proven useful in conjunction with our studies for Paper D and is defined as follows:

$$IMP = \frac{256}{\sum_i WF_i} \cdot 2 \cdot 10^{-13} \tag{4.4}$$

The shape of the waveform is determined by the properties of the scattering surface. Representative waveforms of open ocean, leads, first-year and multiyear sea ice have been selected from SAR mode data of CryoSat-2 and are shown in Figure 4.3. Figure 4.4 shows the normalised power waveforms that allows a comparison of the waveform width. Open ocean waveforms are characterised by a low peak power and a considerable amount of power in the tail of the waveform. The relatively high surface roughness of the ocean reduces the return from the nadir direction while it increases the ones from off-nadir directions. Stack standard deviation is therefore high for waveforms from open ocean and is characteristic

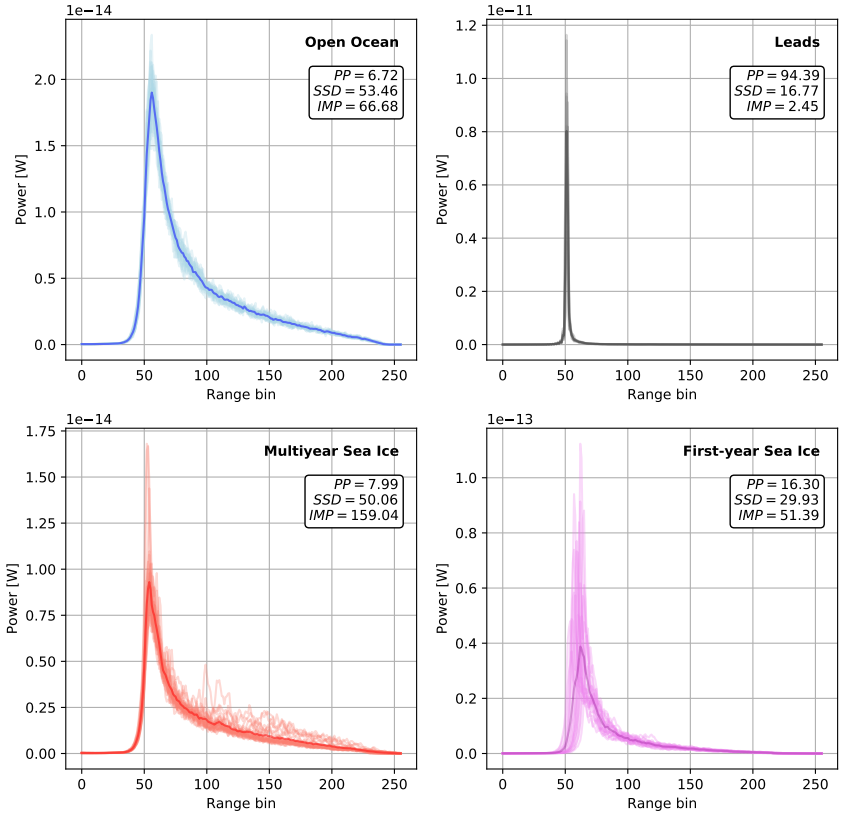

Figure 4.3: *Representative CryoSat-2 altimeter waveforms for open water (upper left), leads (upper right), multiyear sea ice (lower left) and first-year sea ice (lower right). Note the different scaling of the y-axes. Parameters in the annotation box are pulse peakiness(PP), stack standard deviation (SSD) and inverse mean power (IMP).*

for diffuse scattering. The shape of waveforms over open ocean depends on the significant wave height, i.e the waveform is broadened and decreases in peak power with increased wave height [94]. Leads usually have a smooth surface due to their relatively small size and hence little wind fetch or due to the formation of a thin ice layer. The altimeter return is strong and narrow with very little power in the tail [95]. The stack standard deviation is very low because specular reflection reduces the backscatter away from nadir direction. The maximum power of a lead waveform can separate those returns from lead like waveforms, e.g. from mixed surface areas [96]. Sea ice causes a waveform that has a distinct peak with some power in the trailing edge. The different electrical and physical properties of first-year and multiyear sea ice induce differences in their altimeter waveforms. First-year sea ice has a higher peak power but less energy in the tail compared to multiyear ice.

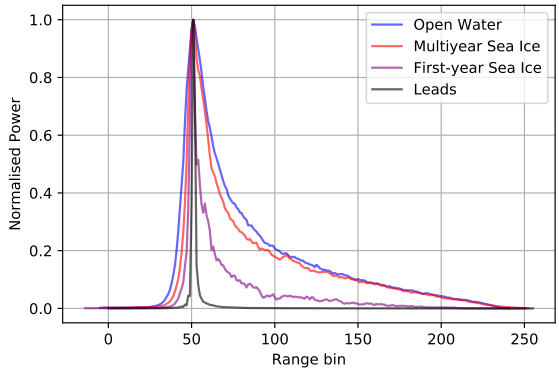

Figure 4.4: *Normalised waveforms for open ocean, leads, first-year and multiyear sea ice.*

The increased peak power is a result of the relatively smoother surface of first-year sea ice. Volume and rough surface scattering reduce the backscattered power at nadir but increase it off-nadir and hence multiyear waveforms contain more power in the tail of their waveform. They are therefore akin to open ocean waveforms. The difference in waveform width is enhanced by comparing their normalised power. The width decreases from open ocean over multiyear and first-year sea ice to leads as shown in Figure 4.4. Furthermore, it is apparent from Figure 4.3 that sea ice waveforms of consecutive acquisitions (light colours in the figure) are much more varying over sea ice. This reflects the variability of the ice surface. In terms of backscattered power, altimeters have oppositional characteristics compared to SAR imagery because of the difference in viewing geometry.

The representative waveforms of Figure 4.3 assume a homogeneous surface within the footprint but this does not always hold true for sea ice surfaces and the size of spaceborne radar altimeters footprints. Especially specular reflectors like smooth ice areas that only cover a small percentage of the footprint area can dominate the returned waveform [97]. Furthermore, if these specular reflectors are located off-nadir they can introduce a range bias that affects the retrieval of the freeboard estimate [98, 99]. Mixtures of different ice types or significant topography from ridges can lead to complex waveforms that impede the identification of the correct position of the nadir return on the leading edge [100]. Figure 4.5 shows an example of a complex waveform over relative homogeneous multiyear sea ice with old refrozen melt ponds. The leading edge on waveform 502 is broadened by a stronger reflector away from nadir while preceding and successive waveforms keep a distinct first peak. The range bias causes an implausible low freeboard estimate that can be eliminated by post-processing. The cause of the waveform distortion cannot be inferred from the near-coincidental SAR image with a resolution of about 100 m. Non regular waveforms, e.g. those with kinked edges, broadened leading edge or multiple peaks, are therefore often discarded from analysis to avoid inaccurate freeboard estimates [42].

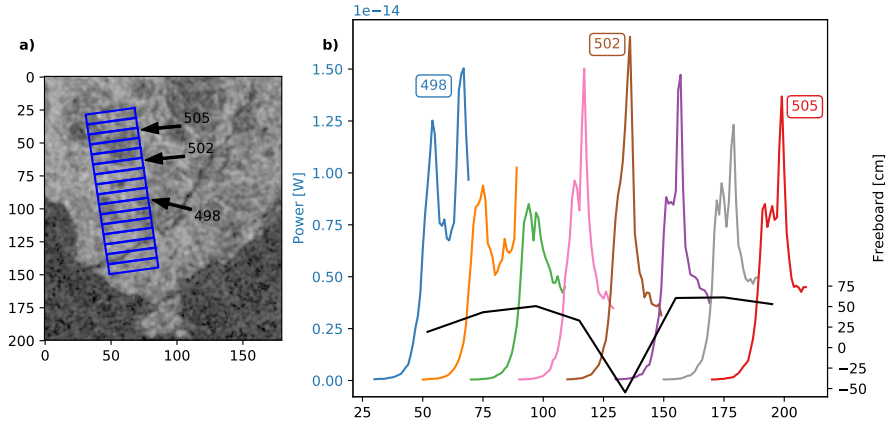

Figure 4.5: *Waveform snagging for a series of altimeter waveforms over a multiyear sea ice floe 2018-02-18. a) SAR HV image with altimeter footprints in blue and b) leading edge of the consecutive waveforms. [Contains Copernicus Sentinel data 2018](from Paper D)*

The presence of a snow cover affects the shape of the waveform and thus most likely also the retracking point. A thicker snow layer broadens the expected waveform and shifts the retracking point closer to the air/snow interface [101, 102]. Though the impact of the snow cover on altimeter waveforms is undisputable, the unavailability of snow property information with high spatio-temporal resolution [103] limits possibilities to take this effect into account for most of the recorded altimeter waveforms.

4.3 Altimeter Missions and Data

Currently there are two spaceborne missions with delay/Doppler altimeters that can provide high resolution data of sea ice freeboard: CryoSat-2 and Sentinel-3 A/B.

CryoSat-2 was the first spaceborne altimeter mission to employ the delay/Doppler technique to reduce the along track footprint size. It was launched in 2010 and is still in operation (2020). The mission is dedicated to determine parameters of the cryosphere, e.g. sea ice freeboard and thickness as well as changes of the large ice sheets of Greenland and Antarctica. It is the only altimeter that provides data coverage up to 88° and therefore of most of the Arctic and Antarctica.

The SIRAL radar instrument onboard CryoSat-2 operates at K_u-band with a centre frequency of 13.575 GHz or equivalently a wavelength of about 2.2 cm. The pulse limited footprint size is 1.65 km in across-track and 300 m in along-track direction after applying delay/Doppler corrections. One waveform covers approximately 15 km in across-track width. The range resolution is about 47 cm and the range window of the waveforms covers approximately 60 metre with 256

Table 4.1: Important parameters for CryoSat-2 and Sentinel-3 altimeters.

Sensor	Coverage	Centre frequency [GHz]	Bandwidth [MHz]	Footprint (across × along)
CryoSat-2	88°	13.575	320	1.6 km×300 m
Sentinel-3	81°	13.575	350	1.6 km×300 m

samples. Parameters of CryoSat-2 altimeter instrument can be found in the products handbook [88].

Sentinel-3 is a constellation of two satellites that both carry among other instruments delay/Doppler radar altimeters. The satellites were launched in 2016 and 2018. However its primary mission objective is not only focused on studies of the cryosphere which is manifested in the higher inclination of the orbit and therefore data coverage only up to approximately 81°. The parameters of the radar altimeter on board Sentinel-3 are very similar to the one of CryoSat-2 with same radar frequency, footprint size and range resolution.

Both missions also offer level-2 data that provide estimates of sea ice freeboard but use slightly different retracking approaches. For CryoSat-2 a model function is fitted to lead waveforms while a threshold retracker is used for sea ice waveforms [88]. Sentinel-3 uses a three-part piecewise exponential function to fit lead as well as sea ice waveforms to obtain the retracking point [104]. Main parameters of the two altimeter systems are summarised in Table 4.1.

5 Ice type Detection and Classification

The increasing availability of radar remote sensing data requires new ways of data handling and processing to fully use the potential of this vast amount of data. Operational ice charting is still a manual process that is time consuming and not able to handle and take into account all available data. For SAR imaging and radar altimeters, there is not only quantitatively more data available but also sensors with different characteristics like frequency and polarisations. Automatic processing and analysis/classification on the one hand and combining different data sources for improved results on the other hand are therefore major areas of ongoing research. This chapter gives a short overview of current developments relevant for sea ice classification with SAR imagery and usage of radar altimeter for detection of different sea ice types to set the work included in this thesis into perspective. Focus is, on the one, hand on dual-polarisation SAR imagery of different frequencies for ice/water classification and, on the other hand, on improving spatial resolution of information from delay/Doppler radar altimeters.

5.1 Sea Ice Type Classification of multi-frequency SAR imagery

SAR imagery delivers high resolution information of the sea ice cover and automatic retrieval of information, e.g. ice edge or ice type, is often desirable to process a large amount of data and reduce the workload on costly manual interpretation. Any classification algorithm needs a set of features that separates the different classes. In the case of sea ice classification from SAR imagery, the appearances of the different ice types and open water described in Section 3.3 need to be represented by a set of parameters. Backscatter intensities in co- and cross-polarisation as well as the polarisation ratio $PR = HV/HH$ commonly represent the image tone. Those alone are, however, not robust discrimination features for sea ice as values for single classes greatly vary in space and time and often overlap [105]. Textural features have been suggested since early automatic classification efforts [106]. One way to quantify image texture is by first- and second-order statistical parameters [107]. First-order parameters include mean, variance, skewness and kurtosis of an image area. Second-order statistics are represented by grey-level co-occurrence matrices (GLCM) and derived statistical parameters [61]. They give information about the spatial distribution of grey values within an image sub-sample. GLCM

texture features are widely used for sea ice classification approaches [108–110]. The large number of potential features and tuning parameters, e.g. window size and grey level quantisation, require feature selection and parameter search. Autocorrelation, defined as follows

$$A(i,j) = \frac{1}{n-1} \frac{\sum_{x,y}(I(x-i,y-j)-\hat{\mu})(I(x,y)-\hat{\mu})}{\hat{\sigma}^2} \tag{5.1}$$

where n is the number of pixels, $\hat{\mu}$ the sample mean value and $\hat{\sigma}$ the sample standard deviation of an image block, is another texture feature used for sea ice classification [28, 111, 112].

Incidence angle dependence impacts the backscatter intensities and can be accounted for as an explicit feature in the classification scheme [28] or imagery can be corrected beforehand [113]. Incidence angle dependence over sea ice can often be approximated by a linear relationship between incidence angle θ and radar backscatter σ^0 in dB [114]:

$$\sigma^0(\theta) \approx m\theta + n. \tag{5.2}$$

where m is the slope and n an offset. Incidence angle slopes can be estimated either by direct calculation from backscatter values or by the difference in incidence angle and backscatter intensity from two observations of the same sea ice area with different incidence angles [115]. Values of incidence angle slopes at co-polarisation are well documented and verified by a number of studies for different sea ice types, e.g. [113, 116, 117]. At cross-polarisation slope values are expected to be lower but reported estimates are limited and inconsistent, e.g. [116, 118, 119]. A better quantification of incidence angle dependence is needed especially for multiyear sea ice. Differences of the noise equivalent sigma zero (NESZ) for Radarsat-2 and Sentinel-1 complicate comparison of obtained values and results need to be verified [120, 121]. Incidence angle correction, i.e. normalisation to a reference angle, has been found to improve the separability of different ice types [117]. Challenges on correction are imposed on image scenes with mixed ice classes because the ice type is usually a-priori unknown.

Once suitable features are identified, a classification scheme needs to be applied that assigns a class or cluster according to the features. In supervised classification the classes have been defined beforehand and the algorithm decides which is the most suitable class for the given set of features. In unsupervised classification the image is clustered into areas of similar feature sets and a class is assigned after clustering. Supervised machine learning techniques like support vector machines and neural networks [122, 123] are nowadays the most popular choices compared to more traditional statistical methods like Bayes and maximum likelihood classifier. All of these methods require an extensive training data set that gives a good representation of the selected classes not only for the training data but also for unknown data. Training sample selection is crucial in all supervised classification methods and inadequate choices can lead to overfitting and the inability to correctly classify unknown data samples. Figure 5.1 gives a schematic view of the classification process.

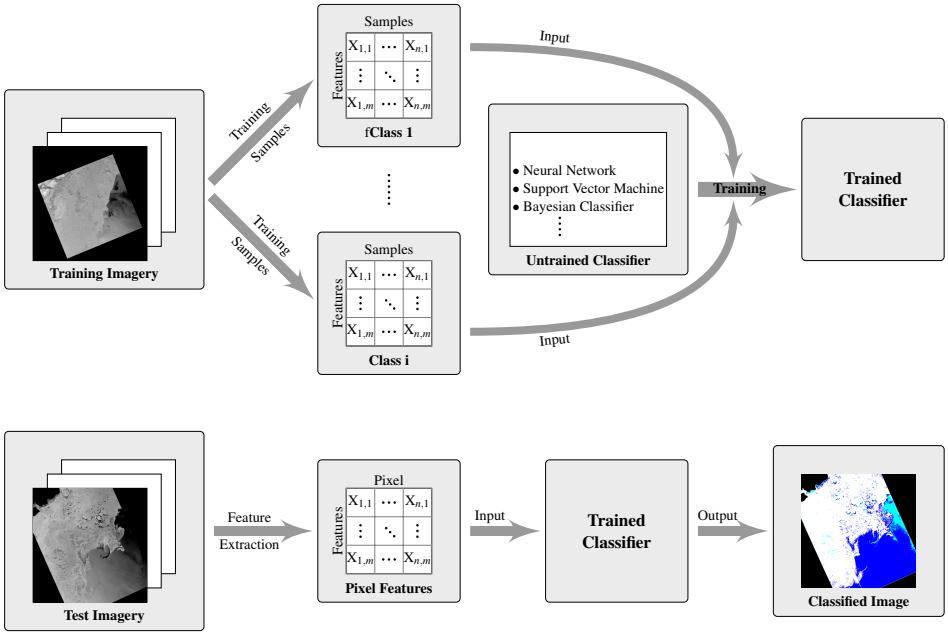

Figure 5.1: *Schematic view of a supervised classification process. Training procedure in the upper row and application of classifier in the lower row.*

Most of the research in sea ice classification is based on C-band imagery as this frequency has been and still is the main source for sea ice information from spaceborne SAR sensors [22]. Though other frequencies and especially L-band have proven to contain complementary sea ice information [69, 70], the limited availability and access to data of those frequencies has impeded implementation of algorithms. L-band polarimetric SAR imagery has been used in a few classification studies to discriminate open water, first-year ice and multiyear ice [39, 124] and in comparison to polarimetric data in X-band and C-band [125]. X-band SAR imagery has also been occasionally used for classification tasks [110, 126]. Studies of polarimetric data usually have a smaller swath width but higher resolution than wide swath SAR imagery. Therefore, the applicability of algorithms need to be adapted and verified for images of lower spatial resolutions [40]. Combination of different frequencies for multi-frequency classification attempts have proven potential from airborne observations [127, 128]. Extensive multi-frequency analysis for spaceborne imagery is, however, hampered by the limited availability of near-coincidental data from different frequency sensors. Time lags of a few hours already introduce a noticeable shift of image features due to the constant motion of the sea ice. Comparison of classification outcomes from different frequencies gives indications on potential benefit of multi-frequency analyses.

5.2 Altimeter Sensitivity to Small Scale Changes of the Ice Surface

Even though the introduction of the delay/Doppler altimeter for spaceborne missions on CryoSat-2 has increased spatial resolution in along-track direction [34], altimeter derived results for sea ice still focus on hemispherical weekly and monthly averaged maps of sea ice thickness [41, 42]. Early studies on Seasat and Geosat altimeter data on the other hand have shown the potential of conventional altimeters to discriminate sea ice types identified with the help of SAR imagery [129–131].

Ice type classification is crucial for correct conversion from sea ice freeboard to thickness (see Equation 4.2). Auxiliary data products such as ice charts or sea ice type products derived from microwave radiometers and/or scatterometers are usually used for this purpose [42]. The resolution of these products is much coarser than the one of the altimeter [132] and small scale variabilities of sea ice surface and/or type are thus lost. The possibilities to discriminate ice types by their differences in altimeter waveform shape (see Section 4.2) have therefore been studied to reduce the dependence on ancillary data [133–137]. Obtained classification results generally agreed well with reference data sets from ice charts and ice type maps but deviations occurred at the transition from one ice type to another and sometimes within the ice pack. The cause of these misclassifications could, however, not be further investigated based on the available ice type information.

SAR imagery is widely used for verification of lead detection algorithms from altimeter waveforms [36, 138, 139], and has proven to be an invaluable source of high resolution reference data. Therefore, the combination of near-coincidental SAR imagery and altimeter waveforms facilitates the identification of sea ice conditions that cause misclassification between ice types in waveform classification algorithms. Furthermore, the response of waveforms to small scale, i.e. a few hundred metres to a few kilometres, variations of the sea ice surface can be investigated to determine the spatial scales on which such features can be resolved in altimeter data. Because sea ice thickness is of greater importance, also the sensitivity of concurrent freeboard estimates related to thickness changes of the ice cover, e.g. ridges or multiyear ice floes, needs to be investigated. Simulations for pulse-limited altimeters have shown a preferential sampling towards thinner ice types and lower ice thickness in cases of mixtures of different sea ice types [100]. A better understanding of waveform behaviour for mixed ice type surfaces is therefore necessary to mitigate these effects.

On the other hand, SAR imagery lacks information about sea ice thickness other than what can be roughly inferred from sea ice type. Assuming similar ice thickness in adjacent areas of the same SAR backscattering characteristics, the linear measurements of sea ice freeboard could be spatially expanded. The research presented in this thesis shows the potential of using SAR imagery and altimeter waveform information to better understand waveform behaviour at mixed ice type areas as well as to identify scales of changes in sea ice surface characteristics needed to obtain meaningful freeboard and thus thickness estimates. Figure 5.2 summarises the potential benefits of the combination of SAR imagery and altimeter waveform

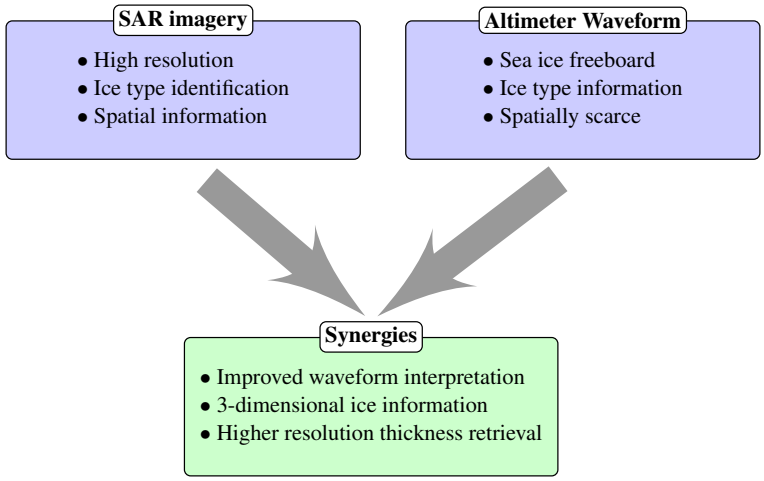

Figure 5.2: *Potential synergies of combination of SAR imagery and altimeter waveforms.*

information.

5.3 Study Areas

Fram Strait located between Greenland and Svalbard and the Beaufort Sea located north of Canada and Alaska are the areas used for the studies within this thesis. Figure 5.3 outlines the location of the study areas within the Arctic and shows the dominating current systems in the respective area.

Fram Strait is of interest because it is the main export gateway of sea ice from the Arctic and thus plays a major role for the ice mass balance of the Arctic [140, 141]. Sea ice is transported from the central Arctic by the Transpolar Drift and finally the East Greenland Current through the Fram Strait while comparatively warm Atlantic Water is transported into the Arctic Ocean by the West Spitzbergen Current [142]. The local currents establish a year round marginal ice zone (MIZ), i.e. the transition from the open ocean into the closed pack ice, within this area [143]. Currents and atmospheric forcing make the ice pack highly dynamic, with relative high sea ice drift speeds of up to a few decimetres/second [144]. SAR imagery offers the temporal and spatial resolution to cover the dynamical processes within the ice pack and the outline of the MIZ.

The Beaufort Sea plays a major role for the creation of old and thick sea ice in the Arctic. The anti-cyclonic (clockwise) circulation of the Beaufort Gyre retains the sea ice within the Arctic Basin for time spans of years where it can thicken and age over time [145, 146]. The transport of multiyear sea ice from the central Arctic into the Beaufort Sea creates a sea ice cover that contains first-year as well as multiyear sea ice [147]. The radar backscatter contrast especially at C-band between old sea ice and first-year sea ice therefore makes the Beaufort Sea an

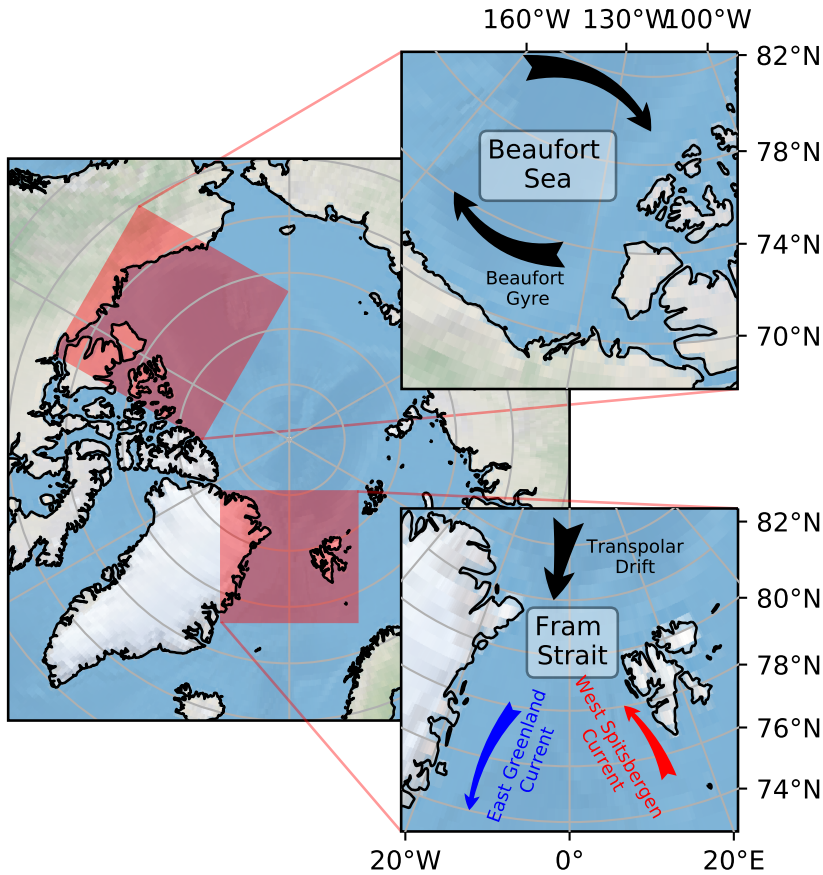

Figure 5.3: *The Arctic with the location of the two study areas Fram Strait and Beaufort Sea and their dominating currents.*

interesting area to investigate the impact of different sea ice types on altimeter waveforms where SAR imagery can be used to verify the ice type. Furthermore, recently observed loss of multiyear ice in this area impacts the distribution of old and thick sea ice in the entire Arctic [148, 149]. Hence, the current and past sea ice situation as well as future changes are of great interest to better understand climate induced changes in this area.

6 Summary of Appended Papers

This chapter gives a short summary of the papers appended to this thesis. The first two papers focus on sea ice concentration estimation and ice/water discrimination from SAR imagery of recent spaceborne SAR systems. The third paper investigates the incidence angle dependence of dual-polarisation SAR imagery and image homogenisation. The last two papers investigate the potential of combining SAR imagery and altimeter data for ice type identification and improved waveform interpretation.

6.1 Paper A

In paper A a sea ice concentration algorithm based on Sentinel-1A imagery is presented. The Copernicus Sentinel-1 programme made C-band SAR imagery available for the general public and Sentinel data has since become one of the most important information sources not just for sea ice applications. Furthermore, the long-term strategic observation plan guarantees data consistency and availability in the future. Automatic classification of SAR imagery is of interest to use the full potential of the amount of available data.

An in house available sea ice concentration algorithm for the Baltic Sea was adapted to the newly available Sentinel-1 data as well as to the study region in the Fram Strait [112]. A neural network is employed to map image features to ice concentrations. Selected image features are HV intensity, HH and HV autocorrelation and incidence angle. Autocorrelation is chosen as a texture feature because it can distinguish the homogeneous texture of open water and brash ice of lower concentration in the marginal ice zone from the more textured closed pack ice. The incidence angle is included to account for variations in backscatter intensities with the incidence angle. The neural network is a simple feed-forward network with one hidden layer consisting of four neurons. The algorithm has been trained with ice charts from the Norwegian Meteorological Institute.

The algorithm is generally able to clearly identify the ice edge. Open water areas within the pack ice are assigned with relatively low concentration values and are therefore correctly identified. Areas of smooth thinner ice that have a homogeneous texture and relative low backscatter are assigned low concentration values even though they represent a completely closed ice surface. Close to the ice edge lower concentration values occur where the ice chart indicates a closed

ice pack. In these areas the backscatter is smooth in texture with relative high values. This is typical for floe sizes below the SAR resolution and differences to the ice chart might be caused by the subjective interpretation of the ice analyst. Generally the algorithm produces results similar to the ice charts and is able to accurately discriminate sea ice areas and open water.

6.2 Paper B

L-band SAR imagery has only been sparsely used for sea ice classification tasks and the first step in algorithm development is the distinction of sea ice and open water. In this paper identical neural networks are trained for ice/water discrimination of dual-polarisation wide swath SAR imagery at C- and L-band. Near-coincidental imagery enables direct comparison of the obtained classification results to analyse similarities, differences and possible synergies in using the two different frequencies. The study area is the Fram Strait located between Greenland and Svalbard and the study period was between October 2014 and March 2016. This area contains a highly variable ice edge year round that offers good possibilities to study ice/water discrimination under different conditions. The dynamics of the ice pack in this region requires near-coincidental observations from different sensors as already time gaps of a few hours introduce noticeable differences between acquisitions.

C-band data used in this study are dual-polarisation Sentinel-1A/B imagery in extra wide swath mode, while L-band data stems from ALOS-2 PALSAR-2 in dual-polarisation ScanSAR mode. Dual-polarisation imagery enhances ice/water discrimination. Imagery was calibrated to γ^0 to reduce the effect of incidence angle on backscatter intensities. The cross-polarisation channel of both frequencies contains image artefacts due to noise (C-band) and low backscatter intensities (L-band). Extracted image features were backscatter intensities at co- and cross-polarisation, the polarisation ratio HV/HH, autocorrelation for cross-polarisation as texture feature and the incidence angle. The features were mapped into three different ice classes, namely ice, open water and thin ice/calm water, using a feed-forward neural network with one hidden layer containing four neurons. The network was trained with manually selected samples from a set of training images representing the three chosen classes.

The algorithm performance is validated against ice charts from the Norwegian Meteorological Institute and ice concentration maps from passive microwave radiometry provided by the University of Bremen. The main differences are observed in the marginal ice zone. Ice charts omit small details during the creation process that are well picked up by the higher resolution SAR images. The ice/water boundary in radiometer derived charts, set to 15 % ice concentration, and the lower resolution slightly shift the ice edge. Features of thin ice/calm water within the ice pack identified by the algorithm show a lower ice concentration in the reference data, but are not well represented due to the lower resolution. Comparison between C-band and L-band data shows similar results with slightly more robust classification at C-band while L-band better distinguishes between open water and thin ice/calm water within the ice pack. For high resolution imagery, ice drift already impacts

the position of small scale features within a short time period, while no significant change could be observed in the reference data.

6.3 Paper C

Incidence angle as an input parameter for sea ice classification has proven to improve the obtained results in Paper B. Preferential imaging on one orbital direction, i.e. ascending or descending, can cause training of the classifier towards spatial ordering of classes instead of the physical properties of the ice types. Incidence angle normalisation to a reference angle before classification can homogenise backscatter intensities over the image swath and thereby improve automatic and visual image interpretation. Incidence angle dependence differs for different ice types and needs to be estimated to perform incidence angle normalisation. In this paper we investigated the incidence angle dependence of Sentinel-1 EW imagery for smooth and rough first-year and multiyear sea ice during the winter period 2016/2017. The incidence angle range of this imagery spans from 19–47°, but for most estimates only the range between 29–47° has been used to avoid data from the first subswath. The incidence angle dependence at cross-polarisation was of particular interest for this study, as values reported in the literature are sparse and inconsistent.

Difference in incidence angle and backscatter intensity in dB between an ascending and descending image is used to obtain a linear relationship for incidence angle dependence. This method is more robust than direct fitting of incidence angle vs. backscatter intensity that needs to account for intra ice type variability. The samples were manually selected thereby accounting for the sea ice drift between the two acquisitions of about 14 h. The study area was located in the eastern Beaufort Sea that offers a good separation between first-year and multiyear sea ice areas.

The obtained slopes for the different ice types at cross-polarisation range from $-0.16\,\mathrm{dB}/1°$ to $-0.04\,\mathrm{dB}/1°$ for smooth first-year sea ice to older multiyear sea ice. Backscatter intensities for smooth ice are close to or at the noise floor of Sentinel-1 images. Thus, they most likely follow the noise floor that is varying from subswath to subswath rather than the actual incidence angle dependence. Values at co-polarisation vary from $-0.24\,\mathrm{dB}/1°$ to $-0.1\,\mathrm{dB}/1°$ for smooth sea ice to old multiyear sea ice. Good agreement with reported incidence angle dependence at co-polarisation increase confidence to the cross-polarisation slopes. The overlay of near- and far-range clippings shows that incidence angle correction reduces the image contrast at the borders particularly for a scene dominated by first-year sea ice. The effect is not so pronounced for multiyear sea ice but still recognisable.

This study demonstrated that incidence angle correction at cross-polarisation should be considered for classification tasks to homogenise the appearance of the sea ice. The difference of incidence angle between different ice types also imposes challenges on the normalisation process if a scene comprises several ice types. A priori knowledge of the ice type is usually not available and using the mean would always be a compromise for all ice types.

6.4 Paper D

SAR imagery provides high resolution 2-dimensional information about the sea ice cover but lacks accurate measures of sea ice thickness to complete the 3-dimensional picture. These information can be provided by radar altimeter data that has so far not extensively been used for small scale investigations of sea ice surface changes. Combining these two different kinds of sensors does not only complement sea ice information but also provides sea ice types information needed for freeboard to thickness conversion. The Copernicus Sentinel mission not only provides C-band SAR imagery but also K_u-Band delay/Doppler altimeter data up to 81.5°N. CryoSat-2 has shown its capabilities to distinguish different ice types by waveform analysis. This study aimed to investigate the altimeter waveform behaviour over different ice types for Sentinel-3 altimeter data validated based on SAR imagery from Sentinel-1. The Beaufort Sea was chosen as the study area because it provides a good mixture of first-year and multiyear sea ice as well as the transition between these two ice types.

The study used C-band SAR imagery in extra-wide swath mode and Sentinel-3 level 1b altimeter data. The time lag between acquisitions was about 5 h, with Sentinel-1 preceding Sentinel-3. Two test cases in January and February 2018 were studied. Ice types were manually identified in the SAR imagery based on backscatter intensities, texture and auxiliary information from ice charts. Peak power, pulse peakiness and stack standard deviation were used to characterise the altimeter waveforms. Histograms of these parameters for first-year and multiyear sea ice showed a principal separation in their distributions but also a non negligible overlap. From comparison with SAR imagery it is evident that multiyear ice floes embedded in first-year sea ice are clearly distinct in the waveform parameters. Mixed ice types between thick first-year and multiyear ice were more similar to waveforms from first-year sea ice.

Knowledge of ice type is crucial for freeboard to thickness conversion and SAR imagery can serve to provide this information in high resolution to improve the thickness retrievals. Furthermore, this study showed the potential to investigate the sensitivity of altimeter waveforms to small scale changes of the sea ice surface. The reduced footprint size of delay/Doppler altimeters has improved lead detection and thus the estimation of the sea surface reference. Despite this increase in spatial resolution, most of the altimeter products are still hemispherical weekly and monthly averages.

6.5 Paper E

This paper continues and deepens the work started in paper C. The relatively large time separation of Sentinel-1 and Sentinel-3 data did not provide the best prerequisites for high resolution comparison of SAR and altimeter data. Smaller time lags in the Beaufort Sea can be achieved by comparison between Sentinel-1 and CryoSat-2 data. The aim of this paper is to investigate the altimeter sensitivity to changes of the sea ice surface in the order of a few hundred metres like large

ridge fields and multiyear sea ice floes embedded in first-year sea ice.

Thirty six Sentinel-1 image sequences containing up to three single extra-wide swath SAR images were compared to near-coincidental CryoSat-2 altimeter tracks. Samples of first-year sea ice, multiyear sea ice and large leads were manually identified in the SAR imagery in the same manner as in paper C. Additionally, samples that showed a high peak power in the altimeter waveform but seemed to have a homogeneous ice type in the SAR image were excluded to avoid effects of sub-resolution smooth areas on the waveform. Samples of three winter seasons, 2015/16, 2016/17 and 2017/18, were taken. The uneven distribution of samples in terms of season and geographical location made a thorough analysis of seasonal changes impossible. Waveform parameters extracted from the data were pulse peakiness, stack standard deviation and inverse mean power. The latter parameter enhanced the contrast between ice types if peak power became similar for different ice types. Peak power was additionally used in the manual interpretation of the data. Freeboard estimates from CryoSat-2 level2 data were used to investigate the possibilities to derive thickness estimates for small scale features.

Histograms of the waveform parameters showed similar results to paper C and the literature. While the ice types are principally distinguished, the large overlap impedes a general robust classification. Analysing the altimeter tracks and the SAR imagery, it is found that waveform changes are coincident with local changes of the sea ice surface as observed from SAR imagery. Lead detection is a standard procedure in altimeter data processing and leads are easily identified by their large peak power. Multiyear sea ice flows of a few kilometres in size cause a distinct drop in peak power from the surrounding first-year sea ice. They need, however, to be significantly larger, about 10 km, to obtain robust estimate of freeboard. Smaller multiyear floes and larger ridges cause a respond in the waveform, but no corresponding change in freeboard is observable. Mixtures of ice types, for example in the transition form on ice type to another, often cause negative freeboards because the leading edge is distorted by the smoother part.

This paper demonstrates the sensitivity of altimeters waveforms to changes of the sea ice surface and thus to better use the resolution improvements of delay/Doppler altimeters. Combination with SAR imagery offers the possibility to better understand waveform behaviour for mixed ice types and to develop retracking algorithms that better accommodate distorted leading edges. Furthermore, high resolution information about sea ice types could also improve the freeboard to thickness conversion.

7 Conclusions and Outlook

The main objective of the thesis was the investigation of multi-frequency and multi-sensor approaches of radar remote sensing techniques to identify complementary information and potential synergies for sea ice observations and monitoring. Research on multi-frequency approaches focused on wide swath C- and L-band SAR imagery for ice type classification and ice/water classification in particular. Multi-sensor approaches combined radar altimetry data and SAR imagery to investigate, on the one hand, the sensitivity of altimeter waveforms to small scale variations of the sea ice surface and, on the other hand, the potential to complete the 3-dimensional picture of the sea ice cover at higher resolutions.

The developed ice/water classification algorithm, trained separately for each respective frequency, operates on wide swath dual-polarisation SAR imagery from Sentinel-1 (C-band) and ALOS-2 PALSAR-2 (L-band). The classification results demonstrate that ice/water discrimination is feasible for both frequencies with good accuracy compared to reference data from ice charts and microwave radiometers. L-band data can therefore complement lacking data at C-band or improve time resolution of observations. Complementary information at these two frequencies showed potential to improve separation of thin ice/calm water areas within the ice pack. Strong sea ice drift, however, impedes direct combination of the two data sets even for relatively short time lags of a few hours between the acquisitions. Therefore, exploitation of multi-frequency wide swath SAR imagery improves sea ice information retrieval but also requires a joint effort of simultaneous acquisition strategies.

Incidence angle dependence of radar backscatter is an intrinsic property of SAR images that can impede their interpretation. In the classification algorithm this effect was mitigated by using γ^0 backscatter intensities and incidence angle as an input parameter. The latter bears the risk that spatial distribution of samples can affect the classification result. Normalising the SAR backscatter to a reference angle can circumvent the problem but requires the knowledge of incidence angle dependence. The study on dual-polarisation C-band imagery closed the gap of missing estimates at cross-polarisation especially for multiyear sea ice and demonstrates that incidence angle normalisation should not only be performed at co- but also at cross-polarisation. A younger and thinner sea ice cover in the future will enhance the benefit of incidence angle correction.

Comparison of SAR imagery and radar altimetry demonstrated the sensitivity

of altimeter waveforms to small scale (on the order of a few hundred metres to a few kilometres) variations of the sea ice surface and therefore the potential to derive sea ice thickness information with higher spatial resolution. Freeboard estimates, however, did not respond accordingly and underline the necessity of retracking methods that better accommodate waveforms of heterogeneous ice type composition within the altimeter footprint. SAR imagery aids the identification of sea ice type necessary for freeboard to thickness conversion and areas where mixtures of ice types can occur within the altimeter footprint. Fully-focused processing of altimeter data has the potential to further improve the along-track resolution and thus improve detection of small leads as well as uncertainties introduced by mixed ice surfaces [150]. Neither processing technique can resolve the lack of information about the snow cover but dual-frequency altimeter measurements can potentially provide such information in the future [103]. On the other hand, the 1-dimensional ice thickness could be expanded spatially by assuming similar sea ice thickness in adjacent regions with uniform SAR backscatter.

The conducted research clearly underlines the benefit of data fusion from different sensors and techniques for sea ice information retrieval but also outlines challenges that need to be overcome to fully exploit the potential in the future. One of the main limitations for operational usage is the availability of near-coincidental acquisitions from different sensors. As opposed to observations over land, the wind and current driven constant motion of sea ice requires near-simultaneous observations to maintain colocation of the data. Future missions such as Radarsat Constellation, ALOS-4, Sentinel-1 C/D, NISAR and potentially Rose-L will increase and ensure the data availability for SAR imagery at different frequencies [151–155]. While SAR observations are settled to provide good coverage of the Arctic, CryoSat-2 is currently the only radar altimeter observing north of 81.5°N. Its limited life span could cause a gap for continuous thickness monitoring of the entire Arctic. CRISTAL, a multi-frequency altimeter mission, might close this gap in the future [156]. Furthermore, it addresses the question of snow thickness retrieval for improved sea ice freeboard estimates.

Data availability and consistency for long-term observations and monitoring of sea ice from space seem assured for the near future. A joint effort of platform operators on the other hand is needed to make more near-simultaneous observations available for operational use as well as research activities. Synchronous observations and a raising number of platforms using similar frequency bands also requires careful observation planning to avoid interference between the sensors [157, 158].

Synergetic exploitation of different data sources also need a close collaboration of the distinct research fields not only from remote sensing but also field and in-situ measurements. The latter ones are necessary to verify the retrieval of geophysical parameters from remotely sensed data and thereby ensuring high quality results. This becomes especially important for sea ice thickness retrievals as currently no other means of measuring large-scale sea ice thickness exist. Moreover, a changing Arctic climate where long-term climatological means of, for example, temperature and snow depth might no longer be valid [159, 160], there will be an increased need of quantifying those changes. One of the primary assumptions of microwave

remote sensing of sea ice is the transparency of the dry cold snow layer during the winter season. Warming events, i.e temporarily increased temperatures up to or above the freezing point, cause melt freeze cycles of the snow layer even during the winter season [161]. Inclusions of ice layers within the snow pack over larger spatial extents might therefore mask out the underlying sea ice from microwave observations. Thereby, the distinction between different ice types by visual and automatic interpretation of SAR imagery might be significantly impeded [29]. Moreover, internal ice layers will also shift the scattering horizon for altimeter measurements away from the snow/ice interface and introduce an additional error to sea ice freeboard measurements [162].

On the algorithm development side, the quickly evolving field of machine learning steadily introduces and improves new classification schemes that are applicable for automatic sea ice interpretation. Numerous studies have been conducted at different areas of the Arctic but are usually limited to that specific area; an overview is given in [22]. Comparability of the classification results is, however, limited by the difference in resolution, used reference and training data as well as the location of the study. Supervised classification schemes are greatly dependent on the quality of the available training data set and algorithms could be made more comparable by a common database of sea ice type samples, either regional or Arctic wide. The increased daily spatial coverage of the Arctic by SAR imagery facilitates the step from a regional to a more global derivation of sea ice parameters. Mosaicking techniques are then needed to fuse imagery from different sensors and different observation geometries [163].

Spaceborne radar remote sensing data has never been more abundant for research activities and consistent long-term observations. This should be exploited to facilitate multi-sensor approaches by a joint effort of the research community and the platform operators. Moreover, the changing Arctic introduces challenges to proven concepts of wintertime microwave remote sensing that require constant evaluation and verification by field and in-situ measurements to ensure high quality results.

Bibliography

[1] G. A. Maykut. "The Surface Heat and Mass Balance". *The Geophysics of Sea Ice*. Ed. by N. Untersteiner. Boston, MA: Springer US, 1986. Chap. 5, pp. 395–463. ISBN: 978-1-4899-5352-0.

[2] J. A. Curry, J. L. Schramm, and E. E. Ebert. Sea Ice-Albedo Climate Feedback Mechanism. *Journal of Climate*, **8**(2) (1995), pp. 240–247. DOI: 10.1175/1520-0442(1995)008<0240:siacfm>2.0.co;2.

[3] R. G. Barry, M. C. Serreze, J. A. Maslanik, and R. H. Preller. The Arctic Sea Ice-Climate System: Observations and modeling. *Reviews of Geophysics*, **31**(4) (1993), pp. 397–422. DOI: 10.1029/93rg01998.

[4] J. C. Comiso and D. K. Hall. Climate trends in the Arctic as observed from space. *Wiley Interdisciplinary Reviews: Climate Change*, **5**(3) (2014), pp. 389–409. DOI: 10.1002/wcc.277.

[5] T. Vihma. Effects of Arctic Sea Ice Decline on Weather and Climate: A Review. *Surveys in Geophysics*, **35**(5) (2014), pp. 1175–1214. DOI: 10.1007/s10712-014-9284-0.

[6] E. Post, U. S. Bhatt, C. M. Bitz, J. F. Brodie, T. L. Fulton, M. Hebblewhite, J. Kerby, S. J. Kutz, I. Stirling, and D. A. Walker. Ecological Consequences of Sea-Ice Decline. *Science*, **341**(6145) (2013), pp. 519–524. DOI: 10.1126/science.1235225.

[7] J. C. Comiso, W. N. Meier, and R. Gersten. Variability and trends in the Arctic Sea ice cover: Results from different techniques. *Journal of Geophysical Research: Oceans*, **122**(8) (2017), pp. 6883–6900. DOI: 10.1002/2017jc012768.

[8] F. Fetterer, K. Knowles, W. Meier, M. Savoie, and A. Windnagel. *Sea Ice Index, Version 3, Sea ice Extent North*. NSIDC: National Snow and Ice Data Center. Boulder, Colorado USA, 2017. DOI: http://dx.doi.org/10.7265/N5K072F8.

[9] J. C. Comiso. Large Decadal Decline of the Arctic Multiyear Ice Cover. *Journal of Climate*, **25**(4) (2012), pp. 1176–1193. DOI: 10.1175/jcli-d-11-00113.1.

[10] R. Kwok. Arctic sea ice thickness, volume, and multiyear ice coverage: losses and coupled variability (1958–2018). *Environmental Research Letters*, **13**(10), 105005 (2018). DOI: 10.1088/1748-9326/aae3ec.

[11] R. Kwok and N. Untersteiner. The thinning of Arctic sea ice. *Physics Today*, **64**(4) (2011), pp. 36–41. DOI: 10.1063/1.3580491.

[12] A. H. H. Renner, S. Gerland, C. Haas, G. Spreen, J. F. Beckers, E. Hansen, M. Nicolaus, and H. Goodwin. Evidence of Arctic sea ice thinning from direct observations. *Geophysical Research Letters*, **41**(14) (2014), pp. 5029–5036. DOI: 10.1002/2014gl060369.

[13] R. Lindsay and A. Schweiger. Arctic sea ice thickness loss determined using subsurface, aircraft, and satellite observations. *The Cryosphere*, **9**(1) (2015), pp. 269–283. DOI: 10.5194/tc-9-269-2015.

[14] P. Rampal, J. Weiss, and D. Marsan. Positive trend in the mean speed and deformation rate of Arctic sea ice, 1979–2007. *Journal of Geophysical Research*, **114**(C5), C05013 (2009). DOI: 10.1029/2008jc005066.

[15] V. M. Eguíluz, J. Fernández-Gracia, X. Irigoien, and C. M. Duarte. A quantitative assessment of Arctic shipping in 2010–2014. *Scientific Reports*, **6**(1), 30682 (2016). DOI: 10.1038/srep30682.

[16] J. Dawson, L. Pizzolato, S. E. Howell, L. Copland, and M. E. Johnston. Temporal and Spatial Patterns of Ship Traffic in the Canadian Arctic from 1990 to 2015. *ARCTIC*, **71**(1) (2018), pp. 15–26. DOI: 10.14430/arctic4698.

[17] W. Dierking. Sea Ice Monitoring by Synthetic Aperture Radar. *Oceanography*, **26**(2) (2013). DOI: 10.5670/oceanog.2013.33.

[18] J. Rouse. Arctic ice type identification by radar. *Proceedings of the IEEE*, **57**(4) (1969), pp. 605–611. DOI: 10.1109/proc.1969.7015.

[19] F. T. Ulaby, R. K. Moore, and A. K. Fung. *Microwave Remote Sensing, Active and Passive: Vol. III*. Artech House, 1986. ISBN: 0890061920.

[20] R. G. Onstott. "SAR and Scatterometer Signatures of Sea Ice". *Microwave Remote Sensing of Sea Ice*. Ed. by F. D. Carsey. American Geophysical Union, 1992. Chap. 2, pp. 73–110.

[21] B. Scheuchl, D. Flett, R. Caves, and I. Cumming. Potential of RADARSAT-2 data for operational sea ice monitoring. *Canadian Journal of Remote Sensing*, **30** (2004), pp. 448–461. DOI: 10.5589/m04-011.

[22] N. Zakhvatkina, V. Smirnov, and I. Bychkova. Satellite SAR Data-based Sea Ice Classification: An Overview. *Geosciences*, **9**(4), 152 (2019). DOI: 10.3390/geosciences9040152.

[23] D. Murashkin, G. Spreen, M. Huntemann, and W. Dierking. Method for detection of leads from Sentinel-1 SAR images. *Annals of Glaciology*, **59**(76pt2) (2018), pp. 124–136. DOI: 10.1017/aog.2018.6.

[24] A. Berg and L. E. B. Eriksson. Investigation of a Hybrid Algorithm for Sea Ice Drift Measurements Using Synthetic Aperture Radar Images. *IEEE Transactions on Geoscience and Remote Sensing*, **52**(8) (2014), pp. 5023–5033. DOI: 10.1109/tgrs.2013.2286500.

[25] S. Muckenhuber and S. Sandven. Open-source sea ice drift algorithm for Sentinel-1 SAR imagery using a combination of feature tracking and pattern matching. *The Cryosphere*, **11**(4) (2017), pp. 1835–1850. DOI: 10.5194/tc-11-1835-2017.

[26] W. Dierking, O. Lang, and T. Busche. Sea ice local surface topography from single-pass satellite InSAR measurements: a feasibility study. *The Cryosphere*, **11**(4) (2017), pp. 1967–1985. DOI: 10.5194/tc-11-1967-2017.

[27] D. O. Dammann, L. E. B. Eriksson, A. R. Mahoney, H. Eicken, and F. J. Meyer. Mapping pan-Arctic landfast sea ice stability using Sentinel-1 interferometry. *The Cryosphere*, **13**(2) (2019), pp. 557–577. DOI: 10.5194/tc-13-557-2019.

[28] J. Karvonen. Baltic Sea Ice Concentration Estimation Based on C-Band HH-Polarized SAR Data. *IEEE Journal of Selected Topics in Applied Earth Observations and Remote Sensing*, **5**(6) (2012), pp. 1874–1884. DOI: 10.1109/jstars.2012.2209199.

[29] A. M. Johansson, J. A. King, A. P. Doulgeris, S. Gerland, S. Singha, G. Spreen, and T. Busche. Combined observations of Arctic sea ice with near-coincident colocated X-band, C-band, and L-band SAR satellite remote sensing and helicopter-borne measurements. *Journal of Geophysical Research: Oceans*, **122**(1) (2017), pp. 669–691. DOI: 10.1002/2016jc012273.

[30] R. Kwok. Satellite remote sensing of sea-ice thickness and kinematics: a review. *Journal of Glaciology*, **56**(200) (2010), pp. 1129–1140. DOI: 10.3189/002214311796406167.

[31] S. Laxon, N. Peacock, and D. Smith. High interannual variability of sea ice thickness in the Arctic region. *Nature*, **425**(6961) (2003), pp. 947–950. DOI: 10.1038/nature02050.

[32] K. A. Giles, S. W. Laxon, and A. L. Ridout. Circumpolar thinning of Arctic sea ice following the 2007 record ice extent minimum. *Geophysical Research Letters*, **35**(22), L22502 (2008). DOI: 10.1029/2008gl035710.

[33] R. K. Raney. The delay/Doppler radar altimeter. *IEEE Transactions on Geoscience and Remote Sensing*, **36**(5) (1998), pp. 1578–1588. ISSN: 1558-0644. DOI: 10.1109/36.718861.

[34] D. Wingham, C. Francis, S. Baker, C. Bouzinac, D. Brockley, R. Cullen, P. de Chateau-Thierry, S. Laxon, U. Mallow, C. Mavrocordatos, L. Phalippou, G. Ratier, L. Rey, F. Rostan, P. Viau, and D. Wallis. CryoSat: A mission to determine the fluctuations in Earth's land and marine ice fields. *Advances in Space Research*, **37**(4) (2006), pp. 841–871. DOI: 10.1016/j.asr.2005.07.027.

[35] Y. Ye, M. Shokr, S. Aaboe, W. Aldenhoff, L. E. B. Eriksson, G. Heygster, C. Melsheimer, and F. Girard-Ardhuin. Inter-comparison and evaluation of sea ice type concentration algorithms. *The Cryosphere Discussions* (2019). DOI: 10.5194/tc-2019-200.

[36] N. Longepe, P. Thibaut, R. Vadaine, J.-C. Poisson, A. Guillot, F. Boy, N. Picot, and F. Borde. Comparative Evaluation of Sea Ice Lead Detection Based on SAR Imagery and Altimeter Data. *IEEE Transactions on Geoscience and Remote Sensing*, **57**(6) (2019), pp. 4050–4061. DOI: 10.1109/tgrs.2018.2889519.

[37] M. R. Drinkwater, R. Kwok, D. P. Winebrenner, and E. Rignot. Multifrequency polarimetric synthetic aperture radar observations of sea ice. *Journal of Geophysical Research*, **96**(C11) (1991), pp. 20679–20698. DOI: 10.1029/91jc01915.

[38] B. Scheuchl, I. Cumming, and I. Hajnsek. Classification of fully polarimetric single- and dual-frequency SAR data of sea ice using the Wishart statistics. *Canadian Journal of Remote Sensing*, **31**(1) (2005), pp. 61–72. DOI: 10.5589/m04-060. eprint: https://doi.org/10.5589/m04-060.

[39] M. Dabboor, B. Montpetit, S. Howell, and C. Haas. Improving Sea Ice Characterization in Dry Ice Winter Conditions Using Polarimetric Parameters from C- and L-Band SAR Data. *Remote Sensing*, **9**(12), 1270 (2017). DOI: 10.3390/rs9121270.

[40] W. Dierking and J. Dall. Sea Ice Deformation State From Synthetic Aperture Radar Imagery–Part II: Effects of Spatial Resolution and Noise Level. *IEEE Transactions on Geoscience and Remote Sensing*, **46**(8) (2008), pp. 2197–2207. DOI: 10.1109/tgrs.2008.917267.

[41] R. Ricker, S. Hendricks, L. Kaleschke, X. Tian-Kunze, J. King, and C. Haas. A weekly Arctic sea-ice thickness data record from merged CryoSat-2 and SMOS satellite data. *The Cryosphere*, **11**(4) (2017), pp. 1607–1623. DOI: 10.5194/tc-11-1607-2017.

[42] R. L. Tilling, A. Ridout, and A. Shepherd. Estimating Arctic sea ice thickness and volume using CryoSat-2 radar altimeter data. *Advances in Space Research*, **62**(6) (2018), pp. 1203–1225. DOI: 10.1016/j.asr.2017.10.051.

[43] W. F. Weeks and S. F. Ackley. "The Growth, Structure, and Properties of Sea Ice". *The Geophysics of Sea Ice*. Ed. by N. Untersteiner. Springer, Boston, MA, 1986. Chap. 1, pp. 9–164. DOI: 10.1007/978-1-4899-5352-0_2.

[44] S. Haykin. *Remote Sensing of Sea Ice and Icebergs*. Wiley-Blackwell, 1994. ISBN: 0471554944.

[45] D. Notz and M. G. Worster. Desalination processes of sea ice revisited. *Journal of Geophysical Research*, **114**(C5), C05006 (2009). DOI: 10.1029/2008jc004885.

[46] G. Timco and R. Frederking. A review of sea ice density. *Cold Regions Science and Technology*, **24**(1) (1996), pp. 1–6. DOI: 10.1016/0165-232x(95)00007-x.

[47] M. E. Shokr and N. K. Sinha. Arctic sea ice microstructure observations relevant to microwave scattering. *Arctic* (1994), pp. 265–279.

[48] F. T. Ulaby, R. K. Moore, and A. K. Fung. *Microwave Remote Sensing, Active and Passive: Vol II*. Artech House, 1982. ISBN: 0201107600.

[49] F. Ulaby and D. G. Long. *Microwave Radar and Radiometric Remote Sensing*. The University of Michigan Press, 2013. ISBN: 0472119354.

[50] J. Wright. Backscattering from capillary waves with application to sea clutter. *IEEE Transactions on Antennas and Propagation*, **14**(6) (1966), pp. 749–754. DOI: 10.1109/tap.1966.1138799.

[51] K. D. Ward, S. Watts, and R. J. Tough. *Sea clutter: scattering, the K distribution and radar performance*. Vol. 20. IET, 2006.

[52] A. K. Fung and H. J. Eom. Application of a Combined Rough Surface And Volume Scattering Theory to Sea Ice And Snow Backscatter. *IEEE Transactions on Geoscience and Remote Sensing*, **GE-20**(4) (1982), pp. 528–536. DOI: 10.1109/tgrs.1982.350421.

[53] Z. Zhao, W. Lang, A. P. Doulgeris, and L. Chen. Improved LLM methods using linear regression. *2017 IEEE International Geoscience and Remote Sensing Symposium (IGARSS)*. IEEE, 2017, pp. 5350–5353. DOI: 10.1109/igarss.2017.8128212.

[54] R. J. Sullivan. *Radar Foundations for Imaging and Advanced Concepts*. SCITECH PUB, 2004. ISBN: 1891121227.

[55] A. Moreira, P. Prats-Iraola, M. Younis, G. Krieger, I. Hajnsek, and K. P. Papathanassiou. A tutorial on synthetic aperture radar. *IEEE Geoscience and Remote Sensing Magazine*, **1**(1) (2013), pp. 6–43. DOI: 10.1109/mgrs.2013.2248301.

[56] W. G. Carrara, R. S. Goodman, and R. M. Majewski. *Spotlight synthetic aperture radar. Signal processing algorithms*. Boston: Artech House, 1995. ISBN: 0890067287.

[57] C. V. J. Jakowatz, D. E. Wahl, P. H. Eichel, D. C. Ghiglia, and P. A. Thompson. *Spotlight-Mode Synthetic Aperture Radar: A Signal Processing*

Approach: A Signal Processing Approach. SPRINGER NATURE, 1996. ISBN: 0792396774.

[58] I. G. Cumming and F. H. Wong. *Digital processing of synthetic aperture radar data. Algorithms and implementation*. Boston: Artech House, 2005. ISBN: 9781580530583.

[59] M. A. Richards, J. A. Scheer, and W. A. Holm. *Principles of Modern Radar. Vol. 1: Basic principles*. SciTech Publishing Inc, 2010. Chap. 21, pp. 835–891. ISBN: 9781891121524.

[60] F. Argenti, A. Lapini, T. Bianchi, and L. Alparone. A Tutorial on Speckle Reduction in Synthetic Aperture Radar Images. *IEEE Geoscience and Remote Sensing Magazine*, **1**(3) (2013), pp. 6–35. DOI: 10.1109/mgrs.2013.2277512.

[61] R. M. Haralick, K. Shanmugam, and I. H. Dinstein. Textural features for image classification. *IEEE Transactions on systems, man, and cybernetics*, **SMC-3**(6) (1973), pp. 610–621.

[62] H. Wakabayashi, Y. Mori, and K. Nakamura. Sea Ice Detection in the Sea of Okhotsk Using PALSAR and MODIS Data. *IEEE Journal of Selected Topics in Applied Earth Observations and Remote Sensing*, **6**(3) (2013), pp. 1516–1523. DOI: 10.1109/jstars.2013.2258327.

[63] W. Alpers, B. Holt, and K. Zeng. Oil spill detection by imaging radars: Challenges and pitfalls. *Remote Sensing of Environment*, **201** (2017), pp. 133–147. DOI: 10.1016/j.rse.2017.09.002.

[64] K. Topouzelis, S. Singha, and D. Kitsiou. Incidence angle normalization of Wide Swath SAR data for oceanographic applications. *Open Geosciences*, **8**(1) (2016), pp. 450–464. DOI: 10.1515/geo-2016-0029.

[65] F. M. Monaldo, D. R. Thompson, R. C. Beal, W. G. Pichel, and P. Clemente-Colon. Comparison of SAR-derived wind speed with model predictions and ocean buoy measurements. *IEEE Transactions on Geoscience and Remote Sensing*, **39**(12) (2001), pp. 2587–2600. DOI: 10.1109/36.974994.

[66] L. M. H. Ulander, A. Carlström, and J. Askne. Effect of frost flowers, rough saline snow and slush on the ERS-l SAR backscatter of thin Arctic sea-ice. *International Journal of Remote Sensing*, **16**(17) (1995), pp. 3287–3305. DOI: 10.1080/01431169508954631.

[67] M. Arkett, D. Flett, R. D. Abreu, P. Clemente-Colon, J. Woods, and B. Melchior. Evaluating ALOS-PALSAR for Ice Monitoring - What Can L-band do for the North American Ice Service? *IGARSS 2008 - 2008 IEEE International Geoscience and Remote Sensing Symposium*. IEEE, 2008, pp. V -188 –V - 191. DOI: 10.1109/igarss.2008.4780059.

[68] W. Dierking and T. Busche. Sea ice monitoring by L-band SAR: an assessment based on literature and comparisons of JERS-1 and ERS-1 im-

agery. *IEEE Transactions on Geoscience and Remote Sensing*, **44**(4) (2006), pp. 957–970. DOI: 10.1109/tgrs.2005.861745.

[69] W. Dierking and H. Skriver. What is Gained by Using an L-band SAR for Sea Ice Monitoring? *Envisat & ERS Symposium*. Vol. ESA SP-572. 2005.

[70] L. E. Eriksson, K. Borenäs, W. Dierking, A. Berg, M. Santoro, P. Pemberton, H. Lindh, and B. Karlson. Evaluation of new spaceborne SAR sensors for sea-ice monitoring in the Baltic Sea. *Canadian Journal of Remote Sensing*, **36**(sup1) (2010), S56–S73.

[71] J. A. Casey, S. E. L. Howell, A. Tivy, and C. Haas. Separability of sea ice types from wide swath C- and L-band synthetic aperture radar imagery acquired during the melt season. *Remote Sensing of Environment*, **174** (2016), pp. 314–328. DOI: 10.1016/j.rse.2015.12.021.

[72] R. Torres, P. Snoeij, D. Geudtner, D. Bibby, M. Davidson, E. Attema, P. Potin, B. Rommen, N. Floury, M. Brown, I. N. Traver, P. Deghaye, B. Duesmann, B. Rosich, N. Miranda, C. Bruno, M. L'Abbate, R. Croci, A. Pietropaolo, M. Huchler, and F. Rostan. GMES Sentinel-1 mission. *Remote Sensing of Environment*, **120** (2012), pp. 9–24. DOI: 10.1016/j.rse.2011.05.028.

[73] J.-W. Park, A. A. Korosov, M. Babiker, S. Sandven, and J.-S. Won. Efficient Thermal Noise Removal for Sentinel-1 TOPSAR Cross-Polarization Channel. *IEEE Transactions on Geoscience and Remote Sensing*, **56**(3) (2018), pp. 1555–1565. DOI: 10.1109/tgrs.2017.2765248.

[74] R. Piantanida. *Thermal denoising of products generated by the Sentinel-1 IPF*. Tech. rep. MPC-0392. S-1 Mission Performance Centre, European Space Agency, 2017.

[75] Japan Aerospace Exploration Agency. *Change of SAR attenuator setting for ScanSAR cross-polarization mode*. 2018.

[76] G. Brown. The average impulse response of a rough surface and its applications. *IEEE Transactions on Antennas and Propagation*, **25**(1) (1977), pp. 67–74. DOI: 10.1109/tap.1977.1141536.

[77] D. B. Chelton, E. J. Walsh, and J. L. MacArthur. Pulse Compression and Sea Level Tracking in Satellite Altimetry. *Journal of Atmospheric and Oceanic Technology*, **6**(3) (1989), pp. 407–438. DOI: 10.1175/1520-0426(1989)006<0407:pcaslt>2.0.co;2.

[78] D. B. Chelton, J. C. Ries, B. J. Haines, L.-L. Fu, and P. S. Callahan. "Chapter 1 Satellite Altimetry". *Satellite Altimetry and Earth Sciences*. Ed. by L.-L. Fu and A. Cazenave. International Geophysics. Academic Press, 2001, pp. 1–131. DOI: 10.1016/s0074-6142(01)80146-7.

[79] S. Schwegmann, E. Rinne, R. Ricker, S. Hendricks, and V. Helm. About the consistency between Envisat and CryoSat-2 radar freeboard retrieval

over Antarctic sea ice. *The Cryosphere*, **10**(4) (2016), pp. 1415–1425. DOI: 10.5194/tc-10-1415-2016.

[80] I. S. Robinson. *Measuring the Oceans from Space: The principles and methods of satellite oceanography (Springer Praxis Books)*. Springer, 2004. Chap. 11. ISBN: 978-3-540-42647-9.

[81] C. H. Davis. A robust threshold retracking algorithm for measuring ice-sheet surface elevation change from satellite radar altimeters. *IEEE Transactions on Geoscience and Remote Sensing*, **35**(4) (1997), pp. 974–979. DOI: 10.1109/36.602540.

[82] V. Helm, A. Humbert, and H. Miller. Elevation and elevation change of Greenland and Antarctica derived from CryoSat-2. *The Cryosphere*, **8**(4) (2014), pp. 1539–1559. DOI: 10.5194/tc-8-1539-2014.

[83] R. Ricker, S. Hendricks, V. Helm, H. Skourup, and M. Davidson. Sensitivity of CryoSat-2 Arctic sea-ice freeboard and thickness on radar-waveform interpretation. *The Cryosphere*, **8**(4) (2014), pp. 1607–1622. DOI: 10.5194/tc-8-1607-2014.

[84] N. T. Kurtz, N. Galin, and M. Studinger. An improved CryoSat-2 sea ice freeboard retrieval algorithm through the use of waveform fitting. *The Cryosphere*, **8**(4) (2014), pp. 1217–1237. DOI: 10.5194/tc-8-1217-2014.

[85] C. Ray, C. Martin-Puig, M. P. Clarizia, G. Ruffini, S. Dinardo, C. Gommenginger, and J. Benveniste. SAR Altimeter Backscattered Waveform Model. *IEEE Transactions on Geoscience and Remote Sensing*, **53**(2) (2015), pp. 911–919. DOI: 10.1109/tgrs.2014.2330423.

[86] M. Fernandes, C. Lázaro, A. Nunes, and R. Scharroo. Atmospheric Corrections for Altimetry Studies over Inland Water. *Remote Sensing*, **6**(6) (2014), pp. 4952–4997. DOI: 10.3390/rs6064952.

[87] T. Vieira, M. J. Fernandes, and C. Lazaro. Impact of the New ERA5 Reanalysis in the Computation of Radar Altimeter Wet Path Delays. *IEEE Transactions on Geoscience and Remote Sensing*, **57**(12) (2019), pp. 9849–9857. DOI: 10.1109/tgrs.2019.2929737.

[88] European Space Agency. *CryoSat-2 product handbook - Baseline D, C2-LI-ACS-ESL-5319, Revision D1.1*. 2019.

[89] R. Ricker, S. Hendricks, D. K. Perovich, V. Helm, and R. Gerdes. Impact of snow accumulation on CryoSat-2 range retrievals over Arctic sea ice: An observational approach with buoy data. *Geophysical Research Letters*, **42**(11) (2015), pp. 4447–4455. DOI: 10.1002/2015gl064081.

[90] J. King, H. Skourup, S. M. Hvidegaard, A. Rösel, S. Gerland, G. Spreen, C. Polashenski, V. Helm, and G. E. Liston. Comparison of Freeboard Retrieval and Ice Thickness Calculation From ALS, ASIRAS, and CryoSat-2 in the Norwegian Arctic to Field Measurements Made During the N-ICE2015 Ex-

pedition. *Journal of Geophysical Research: Oceans*, **123**(2) (2018), pp. 1123–1141. DOI: 10.1002/2017jc013233.

[91] V. Alexandrov, S. Sandven, J. Wahlin, and O. M. Johannessen. The relation between sea ice thickness and freeboard in the Arctic. *The Cryosphere*, **4**(3) (2010), pp. 373–380. DOI: 10.5194/tc-4-373-2010.

[92] M. Zygmuntowska, P. Rampal, N. Ivanova, and L. H. Smedsrud. Uncertainties in Arctic sea ice thickness and volume: new estimates and implications for trends. *The Cryosphere*, **8**(2) (2014), pp. 705–720. DOI: 10.5194/tc-8-705-2014.

[93] S. Laxon. Sea ice extent mapping using the ERS-1 radar altimeter. *Advances in Remote Sensing*, **3**(2) (1994), pp. 112–115.

[94] C. Gommenginger, C. Martin-Puig, S. Dinardo, R. K. Raney, P. Cipollini, D. Cotton, and J. Benveniste. On the performance of CryoSat-2 SAR mode over water surfaces. *Proc. 'CryoSat Validation Workshop 2011', Frascati, Italy (ESA SP-693)*. 2011.

[95] D. Dettmering, A. Wynne, F. Müller, M. Passaro, and F. Seitz. Lead Detection in Polar Oceans—A Comparison of Different Classification Methods for Cryosat-2 SAR Data. *Remote Sensing*, **10**(8), 1190 (2018). DOI: 10.3390/rs10081190.

[96] A. Wernecke and L. Kaleschke. Lead detection in Arctic sea ice from CryoSat-2: quality assessment, lead area fraction and width distribution. *The Cryosphere*, **9**(5) (2015), pp. 1955–1968. DOI: 10.5194/tc-9-1955-2015.

[97] M. R. Drinkwater. Ku band airborne radar altimeter observations of marginal sea ice during the 1984 Marginal Ice Zone Experiment. *Journal of Geophysical Research: Oceans*, **96**(C3) (1991), pp. 4555–4572.

[98] T. W. K. Armitage and M. W. J. Davidson. Using the Interferometric Capabilities of the ESA CryoSat-2 Mission to Improve the Accuracy of Sea Ice Freeboard Retrievals. *IEEE Transactions on Geoscience and Remote Sensing*, **52**(1) (2014), pp. 529–536. DOI: 10.1109/tgrs.2013.2242082.

[99] J. C. Landy, M. Tsamados, and R. K. Scharien. A Facet-Based Numerical Model for Simulating SAR Altimeter Echoes From Heterogeneous Sea Ice Surfaces. *IEEE Transactions on Geoscience and Remote Sensing*, **57**(7) (2019), pp. 4164–4180. DOI: 10.1109/tgrs.2018.2889763.

[100] R. T. Tonboe, L. T. Pedersen, and C. Haas. Simulation of the CryoSat-2 satellite radar altimeter sea ice thickness retrieval uncertainty. *Canadian Journal of Remote Sensing*, **36**(1) (2010), pp. 55–67. DOI: 10.5589/m10-027. eprint: https://doi.org/10.5589/m10-027.

[101] R. Kwok. Simulated effects of a snow layer on retrieval of CryoSat-2 sea ice freeboard. *Geophysical Research Letters*, **41**(14) (2014), pp. 5014–5020. DOI: 10.1002/2014gl060993.

[102] D. Price, J. Beckers, R. Ricker, N. Kurtz, W. Rack, C. Haas, V. Helm, S. Hendricks, G. Leonard, and P. Langhorne. Evaluation of CryoSat-2 derived sea-ice freeboard over fast ice in McMurdo Sound, Antarctica. *Journal of Glaciology*, **61**(226) (2015), pp. 285–300. DOI: 10.3189/2015jog14j157.

[103] I. R. Lawrence, M. C. Tsamados, J. C. Stroeve, T. W. K. Armitage, and A. L. Ridout. Estimating snow depth over Arctic sea ice from calibrated dual-frequency radar freeboards. *The Cryosphere*, **12**(11) (2018), pp. 3551–3564. DOI: 10.5194/tc-12-3551-2018.

[104] Sentinel-3 Mission Performance Centre. *Level 2 SRAL MWR Algorithm Theoretical Baseline Definition, S3MPC.CLS.PBD.005, Issue: 2.0.* 2019.

[105] M. E. Shokr. Evaluation of second-order texture parameters for sea ice classification from radar images. *Journal of Geophysical Research*, **96**(C6) (1991), pp. 10625–10640. DOI: 10.1029/91jc00693.

[106] D. G. Barber and E. F. LeDrew. Multivariate Analysis of Texture Statistics for SAR Sea Ice Discrimination. *12th Canadian Symposium on Remote Sensing Geoscience and Remote Sensing Symposium,* Vancouver Canada: IEEE, 1989, pp. 759–762. DOI: 10.1109/igarss.1989.578989.

[107] N. Aggarwal and R. K. Agrawal. First and Second Order Statistics Features for Classification of Magnetic Resonance Brain Images. *Journal of Signal and Information Processing*, **03**(02) (2012), pp. 146–153. DOI: 10.4236/jsip.2012.32019.

[108] L.-K. Soh and C. Tsatsoulis. Texture analysis of SAR sea ice imagery using gray level co-occurrence matrices. *IEEE Transactions on Geoscience and Remote Sensing*, **37**(2) (1999), pp. 780–795. DOI: 10.1109/36.752194.

[109] N. Zakhvatkina, A. Korosov, S. Muckenhuber, S. Sandven, and M. Babiker. Operational algorithm for ice–water classification on dual-polarized RADARSAT-2 images. *The Cryosphere*, **11**(1) (2017), pp. 33–46. DOI: 10.5194/tc-11-33-2017.

[110] L. Zhang, H. Liu, X. Gu, H. Guo, J. Chen, and G. Liu. Sea Ice Classification Using TerraSAR-X ScanSAR Data With Removal of Scalloping and Interscan Banding. *IEEE Journal of Selected Topics in Applied Earth Observations and Remote Sensing*, **12**(2) (2019), pp. 589–598. DOI: 10.1109/jstars.2018.2889798.

[111] J. Karvonen, M. Simila, and M. Makynen. Open Water Detection From Baltic Sea Ice Radarsat-1 SAR Imagery. *IEEE Geoscience and Remote Sensing Letters*, **2**(3) (2005), pp. 275–279. DOI: 10.1109/lgrs.2005.847930.

[112] A. Berg and L. E. B. Eriksson. SAR Algorithm for Sea Ice Concentration—Evaluation for the Baltic Sea. *IEEE Geoscience and Remote Sensing Letters*, **9**(5) (2012), pp. 938–942. DOI: 10.1109/lgrs.2012.2186280.

[113] N. Y. Zakhvatkina, V. Y. Alexandrov, O. M. Johannessen, S. Sandven, and I. Y. Frolov. Classification of Sea Ice Types in ENVISAT Synthetic Aperture Radar Images. *IEEE Transactions on Geoscience and Remote Sensing*, **51**(5) (2013), pp. 2587–2600. DOI: 10.1109/tgrs.2012.2212445.

[114] R. Moore, K. Soofi, and S. Purduski. A Rader Clutter Model: Average Scattering Coefficients of Land, Snow, and Ice. *IEEE Transactions on Aerospace and Electronic Systems*, **AES-16**(6) (1980), pp. 783–799. DOI: 10.1109/taes.1980.309003.

[115] M. . Mäkynen, A. T. Manninen, M. H. Similä, J. A. Karvonen, and M. T. Hallikainen. Incidence angle dependence of the statistical properties of C-band HH-polarization backscattering signatures of the Baltic Sea ice. *IEEE Transactions on Geoscience and Remote Sensing*, **40**(12) (2002), pp. 2593–2605. DOI: 10.1109/tgrs.2002.806991.

[116] M. Mäkynen and J. Karvonen. Incidence Angle Dependence of First-Year Sea Ice Backscattering Coefficient in Sentinel-1 SAR Imagery Over the Kara Sea. *IEEE Transactions on Geoscience and Remote Sensing*, **55**(11) (2017), pp. 6170–6181. DOI: 10.1109/tgrs.2017.2721981.

[117] M. S. Mahmud, T. Geldsetzer, S. E. L. Howell, J. J. Yackel, V. Nandan, and R. K. Scharien. Incidence Angle Dependence of HH-Polarized C- and L-Band Wintertime Backscatter Over Arctic Sea Ice. *IEEE Transactions on Geoscience and Remote Sensing*, **56**(11) (2018), pp. 6686–6698. DOI: 10.1109/tgrs.2018.2841343.

[118] H. Liu, H. Guo, and L. Zhang. SVM-Based Sea Ice Classification Using Textural Features and Concentration From RADARSAT-2 Dual-Pol ScanSAR Data. *IEEE Journal of Selected Topics in Applied Earth Observations and Remote Sensing*, **8**(4) (2015), pp. 1601–1613. DOI: 10.1109/jstars.2014.2365215.

[119] A. S. Komarov and M. Buehner. Detection of First-Year and Multi-Year Sea Ice from Dual-Polarization SAR Images Under Cold Conditions. *IEEE Transactions on Geoscience and Remote Sensing*, **57**(11) (2019), pp. 9109–9123. DOI: 10.1109/tgrs.2019.2924868.

[120] *RADARSAT-2 Product Description, RN-SP-52-1238, Issue/Revision 1/14,* tech. rep. Maxar Technologies, 2018.

[121] *Sentinel-1 Product Definition, S1-RS-MDA-52-7440, Issue/Revision 2/7.* Tech. rep. European Space Agency, 2016.

[122] L. Wang. *Support Vector Machines: Theory and Applications.* Springer Berlin Heidelberg, 2005. ISBN: 3540243887.

[123] R. Kruse, C. Borgelt, C. Braune, S. Mostaghim, and M. Steinbrecher. *Computational Intelligence.* Springer-Verlag GmbH, 2016. ISBN: 1447172949.

[124] K.-S. Yang and J.-F. Kiang. Comparison of algorithms and input vectors for sea ice classification with L-band PolSAR data. *Progress In Electromagnetics Research B*, **84** (2019), pp. 1–21. DOI: 10.2528/pierb19010406.

[125] S. Singha, M. Johansson, N. Hughes, S. M. Hvidegaard, and H. Skourup. Arctic Sea Ice Characterization Using Spaceborne Fully Polarimetric L-, C-, and X-Band SAR With Validation by Airborne Measurements. *IEEE Transactions on Geoscience and Remote Sensing*, **56**(7) (2018), pp. 3715–3734. DOI: 10.1109/tgrs.2018.2809504.

[126] R. Ressel, A. Frost, and S. Lehner. A Neural Network-Based Classification for Sea Ice Types on X-Band SAR Images. *IEEE Journal of Selected Topics in Applied Earth Observations and Remote Sensing*, **8**(7) (2015), pp. 3672–3680. DOI: 10.1109/jstars.2015.2436993.

[127] B. Scheuchl, I. Hajnsek, and I. Cumming. Sea ice classification using multi-frequency polarimetric SAR data. *IEEE International Geoscience and Remote Sensing Symposium*. IEEE, 2002, pp. 1914–1916. DOI: 10.1109/igarss.2002.1026298.

[128] J. Lohse, A. P. Doulgeris, and W. Dierking. An Optimal Decision-Tree Design Strategy and Its Application to Sea Ice Classification from SAR Imagery. *Remote Sensing*, **11**(13), 1574 (2019). DOI: 10.3390/rs11131574.

[129] L. M. H. Ulander. Interpretation of Seasat radar-altimeter data over sea ice using near-simultaneous SAR imagery. *International Journal of Remote Sensing*, **8**(11) (1987), pp. 1679–1686. DOI: 10.1080/01431168708954807.

[130] L. Ulander. Observations Of Ice Types In Satellite Altimeter Data. *International Geoscience and Remote Sensing Symposium, Remote Sensing: Moving Toward the 21st Century*. IEEE, 1988, pp. 655–658. DOI: 10.1109/igarss.1988.570403.

[131] F. M. Fetterer, S. Laxon, and D. R. Johnson. A comparison of Geosat altimeter and synthetic aperture radar measurements over east Greenland pack ice. *International Journal of Remote Sensing*, **12**(3) (1991), pp. 569–583. DOI: 10.1080/01431169108929673.

[132] S. Aaboe, L.-A. Breivik, A. Sørensen, S. Eastwood, and T. Lavergne. *OSISAF Global Sea Ice Edge and Type Product User's Manual, OSI-402-c & OSI-403-c, Version 2.3*. 2018.

[133] M. Zygmuntowska, K. Khvorostovsky, V. Helm, and S. Sandven. Waveform classification of airborne synthetic aperture radar altimeter over Arctic sea ice. *The Cryosphere*, **7**(4) (2013), pp. 1315–1324. DOI: 10.5194/tc-7-1315-2013.

[134] M. E. Zygmuntowska. "Arctic sea ice altimetry - advances and current uncertainties". PhD thesis. Norway: University of Bergen, 2014.

[135] E. Rinne and M. Similä. Utilisation of CryoSat-2 SAR altimeter in operational ice charting. *The Cryosphere*, **10**(1) (2016), pp. 121–131. DOI: 10.5194/tc-10-121-2016.

[136] X. Shen, J. Zhang, X. Zhang, J. Meng, and C. Ke. Sea Ice Classification Using Cryosat-2 Altimeter Data by Optimal Classifier–Feature Assembly. *IEEE Geoscience and Remote Sensing Letters*, **14**(11) (2017), pp. 1948–1952. DOI: 10.1109/lgrs.2017.2743339.

[137] S. Shu, X. Zhou, X. Shen, Z. Liu, Q. Tang, H. Li, C. Ke, and J. Li. Discrimination of different sea ice types from CryoSat-2 satellite data using an Object-based Random Forest (ORF). *Marine Geodesy* (2019), pp. 1–21. DOI: 10.1080/01490419.2019.1671560.

[138] F. Müller, D. Dettmering, W. Bosch, and F. Seitz. Monitoring the Arctic Seas: How Satellite Altimetry Can Be Used to Detect Open Water in Sea-Ice Regions. *Remote Sensing*, **9**(6), 551 (2017). DOI: 10.3390/rs9060551.

[139] M. Passaro, F. L. Müller, and D. Dettmering. Lead detection using Cryosat-2 delay-doppler processing and Sentinel-1 SAR images. *Advances in Space Research*, **62**(6) (2018), pp. 1610–1625. DOI: 10.1016/j.asr.2017.07.011.

[140] B. Rudels, H. J. Friedrich, and D. Quadfasel. The Arctic Circumpolar Boundary Current. *Deep Sea Research Part II: Topical Studies in Oceanography*, **46**(6-7) (1999), pp. 1023–1062. DOI: 10.1016/s0967-0645(99)00015-6.

[141] R. Kwok. Fram Strait sea ice outflow. *Journal of Geophysical Research*, **109**(C1), C01009 (2004). DOI: 10.1029/2003jc001785.

[142] E. Carmack, I. Polyakov, L. Padman, I. Fer, E. Hunke, J. Hutchings, J. Jackson, D. Kelley, R. Kwok, C. Layton, H. Melling, D. Perovich, O. Persson, B. Ruddick, M.-L. Timmermans, J. Toole, T. Ross, S. Vavrus, and P. Winsor. Toward Quantifying the Increasing Role of Oceanic Heat in Sea Ice Loss in the New Arctic. *Bulletin of the American Meteorological Society*, **96**(12) (2015), pp. 2079–2105. DOI: 10.1175/bams-d-13-00177.1.

[143] R. A. Shuchman, B. A. Burns, O. M. Johannessen, E. G. Josberger, W. J. Campbell, T. O. Manley, and N. Lannelongue. Remote Sensing of the Fram Strait Marginal Ice Zone. *Science*, **236**(4800) (1987), pp. 429–431. DOI: 10.1126/science.236.4800.429.

[144] L. H. Smedsrud, M. H. Halvorsen, J. C. Stroeve, R. Zhang, and K. Kloster. Fram Strait sea ice export variability and September Arctic sea ice extent over the last 80 years. *The Cryosphere*, **11**(1) (2017), pp. 65–79. DOI: 10.5194/tc-11-65-2017.

[145] W. B. Tucker, J. W. Weatherly, D. T. Eppler, L. D. Farmer, and D. L. Bentley. Evidence for rapid thinning of sea ice in the western Arctic Ocean at the end of the 1980s. *Geophysical Research Letters*, **28**(14) (2001), pp. 2851–2854. DOI: 10.1029/2001gl012967.

[146] J. A. Maslanik, C. Fowler, J. Stroeve, S. Drobot, J. Zwally, D. Yi, and W. Emery. A younger, thinner Arctic ice cover: Increased potential for rapid, extensive sea-ice loss. *Geophysical Research Letters*, **34**(24), L24501 (2007). DOI: 10.1029/2007gl032043.

[147] R. J. Galley, E. Key, D. G. Barber, B. J. Hwang, and J. K. Ehn. Spatial and temporal variability of sea ice in the southern Beaufort Sea and Amundsen Gulf: 1980–2004. *Journal of Geophysical Research*, **113**(C5), C05S95 (2008). DOI: 10.1029/2007jc004553.

[148] J. Maslanik, J. Stroeve, C. Fowler, and W. Emery. Distribution and trends in Arctic sea ice age through spring 2011. *Geophysical Research Letters*, **38**(13), L13502 (2011). DOI: 10.1029/2011gl047735.

[149] R. J. Galley, D. Babb, M. Ogi, B. G. T. Else, N.-X. Geilfus, O. Crabeck, D. G. Barber, and S. Rysgaard. Replacement of multiyear sea ice and changes in the open water season duration in the Beaufort Sea since 2004. *Journal of Geophysical Research: Oceans*, **121**(3) (2016), pp. 1806–1823. DOI: 10.1002/2015jc011583.

[150] A. Egido and W. H. F. Smith. Fully Focused SAR Altimetry: Theory and Applications. *IEEE Transactions on Geoscience and Remote Sensing*, **55**(1) (2017), pp. 392–406. DOI: 10.1109/tgrs.2016.2607122.

[151] A. A. Thompson. Overview of the RADARSAT Constellation Mission. *Canadian Journal of Remote Sensing*, **41**(5) (2015), pp. 401–407. DOI: 10.1080/07038992.2015.1104633.

[152] T. Motohka, Y. Kankaku, S. Miura, and S. Suzuki. ALOS-4 L-Band SAR Mission and Observation. *IGARSS 2019 - 2019 IEEE International Geoscience and Remote Sensing Symposium*. IEEE, 2019, pp. 5271–5273. DOI: 10.1109/igarss.2019.8898169.

[153] R. Torres, S. Lokas, G. D. Cosimo, D. Geudtner, and D. Bibby. Sentinel 1 evolution: Sentinel-1C and -1D models. *2017 IEEE International Geoscience and Remote Sensing Symposium (IGARSS)*. IEEE, 2017, pp. 5549–5550. DOI: 10.1109/igarss.2017.8128261.

[154] P. A. Rosen, Y. Kim, R. Kumar, T. Misra, R. Bhan, and V. R. Sagi. Global persistent SAR sampling with the NASA-ISRO SAR (NISAR) mission. *2017 IEEE Radar Conference (RadarConf)*. IEEE, 2017, pp. 0410–0414. DOI: 10.1109/radar.2017.7944237.

[155] N. Pierdicca, M. Davidson, M. Chini, W. Dierking, S. Djavidnia, J. Haarpaintner, G. Hajduch, G. V. Laurin, M. Lavalle, C. López-Martínez, T. Nagler, and B. Su. The Copernicus L-band SAR mission ROSE-L (Radar Observing System for Europe) (Conference Presentation). *Active and Passive Microwave Remote Sensing for Environmental Monitoring III*. Ed. by C. Notarnicola, N. Pierdicca, F. Bovenga, and E. Santi. SPIE, 2019. DOI: 10.1117/12.2534743.

[156] M. Kern, R. Cullen, B. Berruti, J. Bouffard, T. Casal, M. R. Drinkwater, A. Gabriele, A. Lecuyot, M. Ludwig, R. Midthassel, I. N. Traver, T. Parrinello, G. Ressler, E. Andersson, C. M. Puig, O. Andersen, A. Bartsch, S. L. Farrell, S. Fleury, S. Gascoin, A. Guillot, A. Humbert, E. Rinne, A. Shepherd, M. R. van den Broeke, and J. Yackel. The Copernicus Polar Ice and Snow Topography Altimeter (CRISTAL): Expected Mission Contributions. *The Cryosphere Discuss* (2020). DOI: 10.5194/tc-2020-3.

[157] R. Natsuaki and A. Hirose. Profiles of RFI in Alos-2 Images - A Case Study in Tokyo Bay, Japan. *IGARSS 2018 - 2018 IEEE International Geoscience and Remote Sensing Symposium*. IEEE, 2018, pp. 319–322. DOI: 10.1109/igarss.2018.8518551.

[158] P. Meadows. *Sentinel-1 Long Duration Mutual Interference, MPC-0432, Issue1.0*. S-1 Mission Performance Center, 2018.

[159] J. E. Overland and M. Wang. Recent Extreme Arctic Temperatures are due to a Split Polar Vortex. *Journal of Climate*, **29**(15) (2016), pp. 5609–5616. DOI: 10.1175/jcli-d-16-0320.1.

[160] M. Webster, S. Gerland, M. Holland, E. Hunke, R. Kwok, O. Lecomte, R. Massom, D. Perovich, and M. Sturm. Snow in the changing sea-ice systems. *Nature Climate Change*, **8**(11) (2018), pp. 946–953. DOI: 10.1038/s41558-018-0286-7.

[161] R. M. Graham, L. Cohen, A. A. Petty, L. N. Boisvert, A. Rinke, S. R. Hudson, M. Nicolaus, and M. A. Granskog. Increasing frequency and duration of Arctic winter warming events. *Geophysical Research Letters*, **44**(13) (2017), pp. 6974–6983. DOI: 10.1002/2017gl073395.

[162] G. D. Quartly, E. Rinne, M. Passaro, O. B. Andersen, S. Dinardo, S. Fleury, A. Guillot, S. Hendricks, A. A. Kurekin, F. L. Müller, R. Ricker, H. Skourup, and M. Tsamados. Retrieving Sea Level and Freeboard in the Arctic: A Review of Current Radar Altimetry Methodologies and Future Perspectives. *Remote Sensing*, **11**(7), 881 (2019). DOI: 10.3390/rs11070881.

[163] S. E. L. Howell, D. Small, C. Rohner, M. S. Mahmud, J. J. Yackel, and M. Brady. Estimating melt onset over Arctic sea ice from time series multi-sensor Sentinel-1 and RADARSAT-2 backscatter. *Remote Sensing of Environment*, **229** (2019), pp. 48–59. DOI: 10.1016/j.rse.2019.04.031.